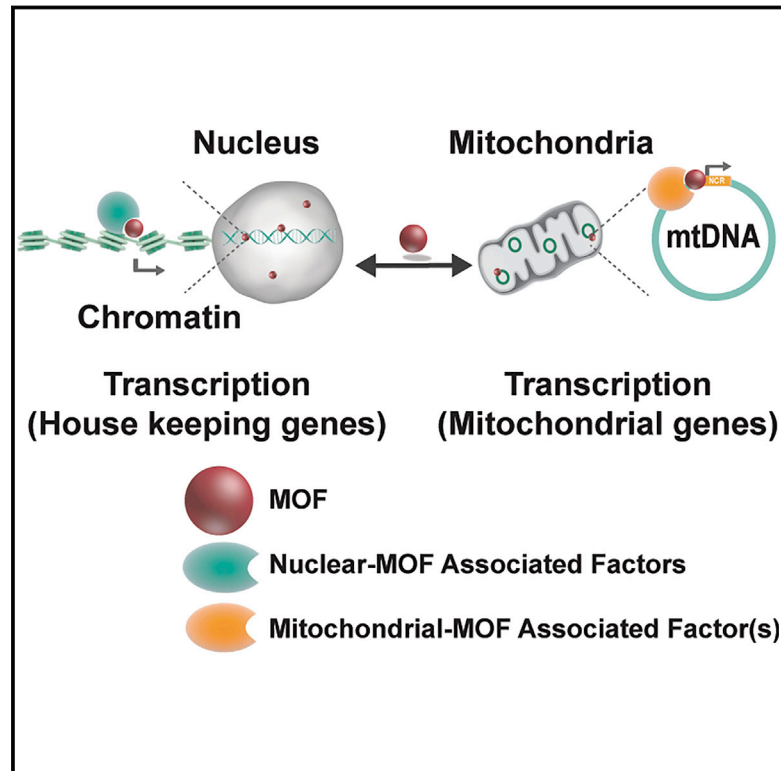


MOF Acetyl Transferase Regulates Transcription and Respiration in Mitochondria

Graphical Abstract



Authors

Aindrila Chatterjee, Janine Seyfferth, Jacopo Lucci, ..., Nikolaus Pfanner, Thomas Becker, Asifa Akhtar

Correspondence

akhtar@ie-freiburg.mpg.de

In Brief

A histone acetyl transferase regulates mitochondrial gene expression.

Highlights

- MOF, KANSL1, and KANSL3 show nuclear and mitochondrial localization
- MOF binds mtDNA, and its loss affects mitochondrial gene expression
- MOF catalytic activity is required to rescue transcriptional and respiratory defects
- *Mof* knockout shows mitochondrial deterioration in cardiomyocytes and cardiac failure



MOF Acetyl Transferase Regulates Transcription and Respiration in Mitochondria

Aindrila Chatterjee,^{1,2} Janine Seyfferth,¹ Jacopo Lucci,¹ Ralf Gilsbach,⁴ Sebastian Preissl,⁴ Lena Böttinger,³ Christoph U. Mårtensson,^{2,3} Amol Panhale,^{1,2} Thomas Stehle,¹ Oliver Kretz,^{5,6} Abdullah H. Sahyoun,¹ Sergiy Avilov,¹ Stefan Eimer,^{2,7} Lutz Hein,^{4,5} Nikolaus Pfanner,^{3,5} Thomas Becker,^{3,5} and Asifa Akhtar^{1,8,*}

¹Max Planck Institute of Immunobiology and Epigenetics, 79108 Freiburg, Germany

²Faculty of Biology

³Institute of Biochemistry and Molecular Biology, ZBMZ, Faculty of Medicine

⁴Institute for Experimental and Clinical Pharmacology and Toxicology, Abteilung II

⁵BIOSS Centre for Biological Signalling Studies

Albert Ludwigs University of Freiburg, 79085 Freiburg, Germany

⁶Renal Division, University Medical Center Freiburg, 79106 Freiburg, Germany

⁷Center for Systems Biology (ZBSA), Albert Ludwigs University of Freiburg, 79085 Freiburg, Germany

⁸Lead Contact

*Correspondence: akhtar@ie-freiburg.mpg.de

<http://dx.doi.org/10.1016/j.cell.2016.09.052>

SUMMARY

A functional crosstalk between epigenetic regulators and metabolic control could provide a mechanism to adapt cellular responses to environmental cues. We report that the well-known nuclear MYST family acetyl transferase MOF and a subset of its non-specific lethal complex partners reside in mitochondria. MOF regulates oxidative phosphorylation by controlling expression of respiratory genes from both nuclear and mtDNA in aerobically respiring cells. MOF binds mtDNA, and this binding is dependent on KANSL3. The mitochondrial pool of MOF, but not a catalytically deficient mutant, rescues respiratory and mtDNA transcriptional defects triggered by the absence of MOF. *Mof* conditional knockout has catastrophic consequences for tissues with high-energy consumption, triggering hypertrophic cardiomyopathy and cardiac failure in murine hearts; cardiomyocytes show severe mitochondrial degeneration and deregulation of mitochondrial nutrient metabolism and oxidative phosphorylation pathways. Thus, MOF is a dual-transcriptional regulator of nuclear and mitochondrial genomes connecting epigenetics and metabolism.

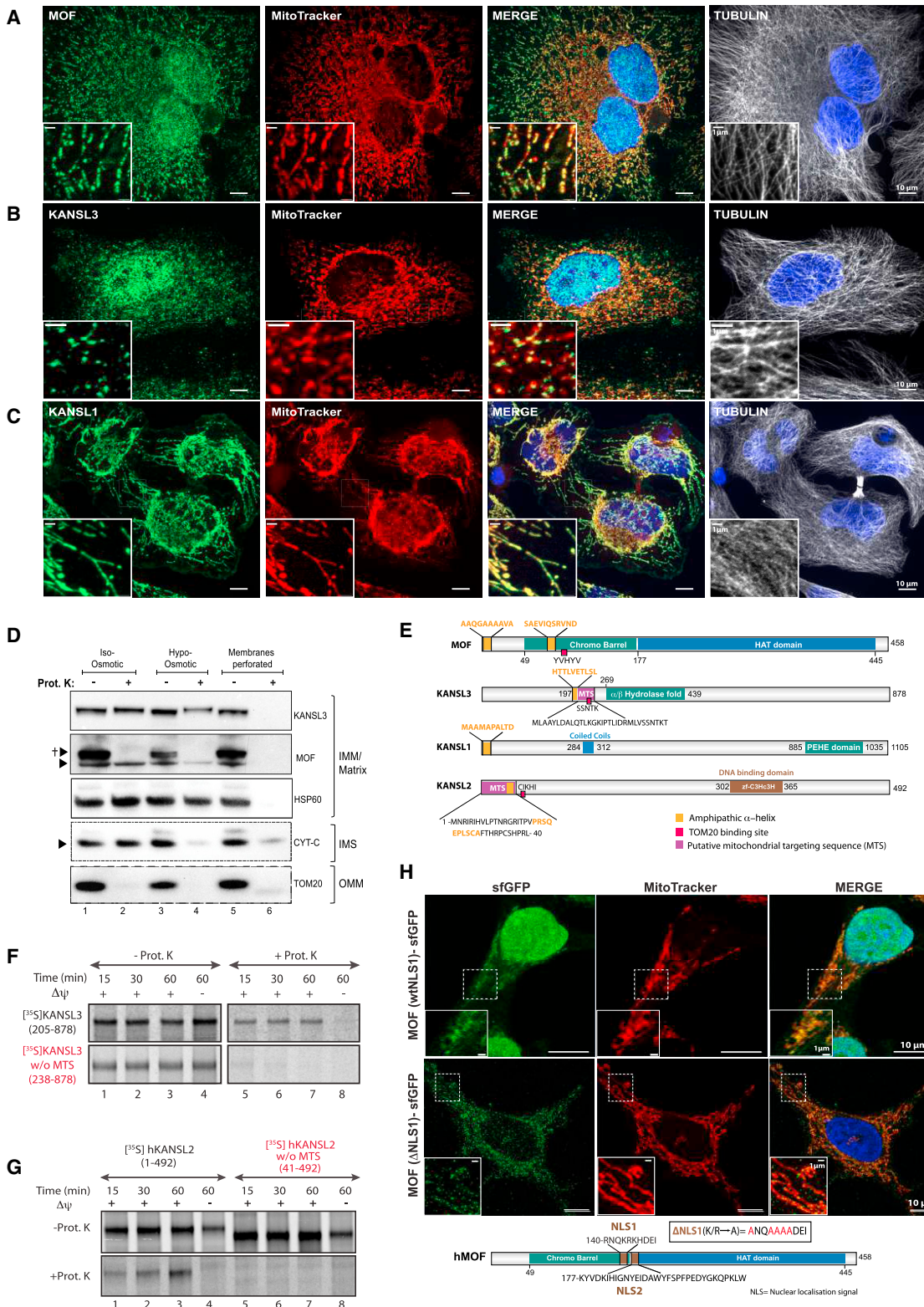
INTRODUCTION

Cells use compartmentalization for functional segregation of major metabolic processes. This relies on an orchestrated communication between the nucleus and cytoplasm. A key metabolic hub in the cytoplasm is the mitochondrion, a unique organelle with genetic contributions from two (nuclear and mitochondrial) genomes. The mammalian mtDNA is circular and is compacted into nucleoids. Transcription of the mtDNA is governed by a

dedicated nuclear-encoded machinery, which includes a RNA polymerase (POLRMT) and is assisted by transcription initiation factors TFB1M and TFB2M (Shutt and Shadel, 2010). TFAM, a major nucleoid component, is also critical for mtDNA transcription and replication. Recently, a number of nuclear transcription factors (e.g., STAT3, CREB, NF- κ B, and MEF2D) have been reported to localize in mitochondria. Such “bi-organellar” transcription factors are often involved in mtDNA (gene) expression, electron transport chain activity, and apoptosis (Szczepanek et al., 2012). However, their possible roles in the coordinated function of the nucleus and mitochondria remain largely unknown.

Interestingly, mitochondria can also influence nuclear transcription by supplying metabolites (such as SAM, Acetyl-CoA, and ATP) that facilitate epigenetic alterations of chromatin structure/dynamics. Reversible histone acetylation is a prominent epigenetic modification playing diverse roles in several cellular processes. In particular, acetylation of lysine 16 of histone H4 (H4K16ac) is important for chromatin de-compaction and transcriptional activation (Shogren-Knaak et al., 2006; Kalashnikova et al., 2013). MOF (males absent on the first; also known as MYST1 or KAT8) is the major lysine acetyl transferase (KAT) responsible for deposition of H4K16ac in flies and mammals (Gu et al., 1998; Hilfiker et al., 1997; Taipale et al., 2005). It resides in distinct, evolutionarily conserved transcription regulatory complexes, namely the MSL (male specific lethal) and the NSL (non-specific lethal) complexes. They dictate MOF’s enzymatic activity and target selection (Cai et al., 2010; Mendjan et al., 2006; Raja et al., 2010). In flies, MOF-MSL complex is involved in regulation of X-chromosomal genes (Conrad and Akhtar, 2011; Lucchesi and Kuroda, 2015). However, association with KANSLs (members of the NSL complex) radically broadens MOFs regulatory spectrum to target constitutively active genes located on all chromosomes, a function that is remarkably conserved from flies to mammals (Chelmicki et al., 2014; Feller et al., 2012; Lam et al., 2012; Ravens et al., 2014).

Despite broad chromatin binding, many of the MOF-targeted genes remain unaffected upon MOF depletion (Chelmicki et al.,



(legend continued on next page)

2014). In fact, MOF can adopt different roles in different contexts (Chen et al., 2014; Kapoor-Vazirani et al., 2008; Li et al., 2009; Sykes et al., 2006), which imply hidden nuances to MOF's molecular functions and an inherent sensitivity to its environment. So, when a classically nuclear KAT like MOF is associated with an array of complex metabolic processes like cell division (Taipale et al., 2005), DNA-damage repair (Gupta et al., 2005), and autophagy (Füllgrabe et al., 2013), it has to be sensitive to cellular cues. The question is how. The most direct way of MOF's rapid response to different information cues would require its intracellular mobility between the nucleus and the metabolic signaling hubs in cytoplasm. This has been previously demonstrated for deacetylases, which play a regulatory role in cellular homeostasis by localizing in different cellular compartments (Backs et al., 2006; Di Giorgio and Brancolini, 2016). However, a "non-nuclear" function of MOF has not been described to date.

In this study, we investigated a possible role of MOF beyond nuclear gene transcription. We detect a significant pool of MOF, as well as members of the NSL complex, KANSL1 and KANSL3, in the mitochondria. Gene-expression analysis of MOF-depleted cells revealed that MOF regulates expression of genes involved in oxidative phosphorylation (OXPHOS) in aerobically respiring cells. Depletion of MOF/KANSL1 causes significant downregulation of mitochondrial DNA (mtDNA) transcription and subsequent translation, leading to impaired cellular respiration. Importantly, mitochondrial transcriptional and respiratory defects can be rescued by a mitochondrially tethered MOF, but not its catalytic mutant (E350Q), indicating that MOF's enzymatic activity is important for mitochondrial function. We demonstrate the relevance of MOF-mediated mitochondrial regulation in vivo by generating a conditional MOF knockout mouse in heart and skeletal muscle. These mice die of acute cardiomyopathy within 3 weeks of birth and show mitochondrial degeneration. Thus, we provide an unprecedented role of MOF acetyl transferase in mitochondrial transcription regulation. By regulating transcription in two cellular compartments, MOF could play an important role in coordinating epigenetic regulation and metabolic control.

RESULTS

MOF, KANSL1, and KANSL3 Are Localized in Mitochondria

We reviewed the sub-cellular distribution of MOF and two KANSL complex members (KANSL1 and KANSL3) by confocal microscopy in HeLa cells and found a significant population of all three proteins in the cytoplasm, in addition to their well-

documented nuclear locale. The cytoplasmic signals were reminiscent of typical organelle staining. To verify this, we co-labeled cells for MOF/KANSL1/KANSL3 along with MitoTracker (which labels mitochondria) and microtubules, two organelles known to form distinct tubular networks in cells. All three proteins showed definitive mitochondrial localization (Figures 1A–1C). MOF and KANSL3 showed homogenous nuclear distribution and the non-nuclear signal largely localized to mitochondria. Interestingly, the signals were punctate and not uniform (Figures 1A and 1B), similar to the staining pattern of certain mitochondrial proteins. KANSL1, however, exhibited homogenous mitochondrial staining (Figure 1C). We further confirmed mitochondrial localization of the proteins using multi-color 3D high-resolution structured illumination microscopy (HR-SIM) and biochemical fractionations (Figures S1A–S1C). Antibody specificity was verified by knockdown studies (Figures S1D, S1E, and S2A–S2C). Interrogation of sub-mitochondrial localization of the KANSL proteins by proteinase K protection assay revealed that KANSL3 was restricted to the inner mitochondrial membrane/matrix (Figure 1D), but MOF showed dual localization at the outer membrane, as well as mitochondrial matrix/inner membrane (Figure 1D, see Discussion). Taken together, these results establish that, in addition to the nucleus, MOF and KANSL3 reside in mitochondria.

KANSL Proteins Possess Mitochondrial-Targeting Signals

Proteins residing in mitochondria frequently contain mitochondrial-targeting sequences (MTS) (Omura, 1998). We thus investigated amino acid sequences of core human NSL members (see STAR Methods) and found putative MTS in KANSL3 and KANSL2 (Figure 1E). To test their functionality, import assays were performed on isolated yeast mitochondria with in-vitro transcribed KANSL3 and KANSL2. Due to technical difficulties of in vitro synthesis of the 878-aa-long KANSL3 protein, we worked with its truncated version, starting from the putative MTS. Remarkably, we found that radiolabeled KANSL3 derivative (205–878 aa) and full-length KANSL2 were imported into isolated mitochondria by several criteria (Figures 1F and 1G). First, the proteins were transported to a protease-protected location. Second, the import occurred in a membrane-potential-dependent manner, which is a hallmark of protein transport to the mitochondrial inner membrane and matrix. Third, removal of the predicted MTS abolished import of KANSL3 (238–878 aa) and KANSL2 (41–492) (Figures 1F and 1G). Finally, the import of [³⁵S] KANSL3 (205–878 aa) was reduced in mitochondria lacking a major preprotein receptor of the translocase of the outer mitochondrial membrane, TOM20 (Figure S3A).

(D) Proteinase K (Prot. K) protection assay of HeLa cell mitochondria. Extent of digestion was determined by blotting for key intra-mitochondrial proteins (HSP60, CYT-C, TOM20). IMM, inner mitochondrial membrane; IMS, inter-membrane space; OMM, outer mitochondrial membrane. Triangles, specific protein. Cross, isoform/post-translationally modified version of the protein. See also Figures S1C–S1E.

(E) Representative diagram of MOF, KANSL3, KANSL1, and KANSL2 with major domains/features (predicted) that are important for mitochondrial localization. (F and G) Import assays were performed using in vitro synthesized (F) [³⁵S] KANSL3 with (205–878)/without (238–878) putative mitochondrial targeting signal (MTS) and (G) [³⁵S] KANSL2 with (1–492)/without (41–492) putative MTS into yeast mitochondria. Samples were treated with +Prot. K and assays were performed with both polarized (+ΔΨ) and depolarized (–ΔΨ) mitochondria. –Prot. K, control (50% intensity in G). The mutant derivatives of respective proteins are denoted in red. See also Figure S3A.

(H) Immunofluorescence images of MOF-sfGFP cell lines with WT (wtNLS1) or mutated nuclear localization (ΔNLS1) signals. MitoTracker was used to stain mitochondria. A schematic representation of human MOF protein containing the predicted nuclear localization signals, NLS1 and NLS2, is shown below.

We could not find a canonical MTS in MOF. However, we could identify a strong nuclear localization signal—NLS1 in MOF (see [STAR Methods](#); [Figure 1H](#), cartoon). We hypothesized that, in the absence of a strong nuclear bias, a cryptic MTS of MOF (if present) would drive its enrichment in mitochondria. We tested this hypothesis by studying intracellular distribution of MOF-sfGFP (superfolder green fluorescent protein; stable cell lines) with wild-type (WT) or mutated NLS1 (Δ NLS1). Remarkably, MOF(Δ NLS1)-sfGFP largely localized to mitochondria, in sharp contrast to the nuclear bias of MOF(wtNLS1)-sfGFP ([Figure 1H](#)). Therefore, in the absence of NLS1, the localization of MOF is swapped from the WT scenario with a newfound bias for the mitochondria over the nucleus, indicating that the presence of buried mitochondrial-targeting information. Taken together, these data demonstrate that MOF, KANSL2, and KANSL3 are bona fide residents of mitochondria and contain mitochondrial-targeting information.

MOF Depletion Affects OXPHOS Gene Expression in Aerobically Respiring Cells

MOF/KANSLs are well-known transcription regulators in the nucleus. Their presence in mitochondria makes it plausible that they may regulate mitochondrial gene expression. In glucose-supplemented media, cells use aerobic glycolysis for energy. However, if grown in galactose, cells switch to mitochondria-based OXPHOS for ATP synthesis and effectively increase their sensitivity to mitochondrial insults ([Robinson et al., 1992](#)). We reasoned that, in case the cellular respiratory strategy is under MOF control, its knockdown might trigger media-dependent alterations in transcriptional regulation of mitochondria. We therefore adapted HeLa cells to glucose/galactose media before performing transcriptome analysis on MOF-depleted cells ([Figure 2A](#)).

We observed a large overlap in the number of deregulated genes in two media sets ([Figure 2A](#), right, marked as I). Of the

commonly affected genes, a majority showed similar expression trends ([Figure 2B](#), scatterplot, gray dots) with few divergent genes ([Figure 2B](#), scatterplot, green dots). Interestingly, OXPHOS genes were downregulated in galactose and remained unaffected in glucose ([Figure 2B](#), left heat map). Analysis of genes selectively deregulated in galactose media ([Figure 2A](#), II from Euler plot) revealed that two of the most significantly affected pathways were OXPHOS ($p = 2.24E-10$) and mitochondrial dysfunction ($p = 3.55E-09$) ([Figure 2C](#), in red). In contrast, similar analysis performed on genes affected exclusively in glucose did not reveal similar findings ([Figure S3B](#)). Importantly, the possibility of an inherent transcriptional bias was ruled out, since there was no significant difference in mitochondrial RNA levels between siSCRAM controls of the two media ([Figure 2D](#)).

So far, we had scored a clear defect in mitochondrial OXPHOS in galactose media. To understand the full impact of MOF knockdown (galactose) on mitochondrial respiration, we generated network maps (see [STAR Methods](#)) of critical mitochondrial regulatory pathways, like mitochondrial biogenesis, organization, morphology, mass, quantity/size, and mtDNA replication ([Figure 2E](#)). We found that—although some key genes, like TFAM, PRDX3, and CAV2 were mildly downregulated—they did not result in significant inhibition (high-confidence prediction) of any of the analyzed pathways. We could predict upregulation of mitochondrial biogenesis and mass, which might be more of a cause than a consequence of OXPHOS gene deregulation. Thus, evaluation (gene expression) of vital pathways influencing mitochondrial respiration did not account for the downregulation of OXPHOS genes, implying a more direct impact of MOF on their transcription.

The OXPHOS machinery is a unique amalgamation of components from two different genomes. While most of its constituent proteins are transcribed from nucleus, few (13) core enzymatic modules are supplemented by the mtDNA. Since our

Figure 2. MOF-Depleted Cells Show Reduced OXPHOS Transcription and Mitochondrial Respiration

(A) Cartoon representation of RNA-seq strategy used on MOF depleted cells. Euler plots represent genes deregulated either specifically in galactose (II, yellow) or glucose (III, blue) or both (I) media conditions.

(B) Central scatterplot shows genes commonly deregulated in both glucose and galactose media (I), from [Figure 2A](#), represented in scatterplot at center (log2 transformed). Genes showing opposing trends in two media sets are highlighted in green, with trends shown in flanking heat maps. Canonical pathways affected in each dataset are shown in boxes below respective heat maps.

(C) Bubble plot presents top 15 pathways specifically affected in galactose media (II, from [Figure 2A](#)). y axis shows Z score of enrichment, and the x axis indicates the ratio of representation of genes of a particular pathway. Bubble size is directly proportional to the significance of discovery ($-\log_{10} p$ value). Mitochondria-associated pathways are highlighted in red. See also [Figure S3B](#).

(D) Violin plots representing log10 reads per kilobase million (RPKM) value of expression of all mitochondrial and oxidative phosphorylation (OXPHOS) genes in glucose (blue) and galactose (yellow) media. Scramble controls from the two media sets were overlaid for analysis.

(E) Analysis of protein networks associated with mitochondrial health in siMOF (galactose) samples. The analyzed mitochondrial pathways are involved in its organization, mass, DNA replication, morphology, biogenesis, quantity, and size.

(F and G) Relative mtDNA transcript levels along with key nuclear encoded mitochondrial regulatory factors in control (siSCRAM, white) and (F) siMOF (red)/(G) siKANSL1 (blue)-treated cells in galactose media. Data represent mean \pm SD of three biological replicates. See also [Figures S3C–S3F](#).

(H) Relative mtDNA levels in control (siSCRAM, gray), siMOF (red hollow bar), and siKANSL1 (blue hollow bar) after normalization to nuclear DNA (nDNA) levels. MT1–3 represent three primers mapping to distinct regions on the mtDNA. Data represent mean \pm SD of three biological replicates.

(I) Scatterplot representation of mitochondrial membrane potential calculated from JC-1-staining of siSCRAM (green), siMOF (red), and siKANSL1 (blue) cells. Data represent mean \pm SEM of five biological replicates. Unpaired *t* test, *** $p < 0.005$. See also [Figure S3G](#).

(J) Left, bioenergetic profiling of siSCRAM (black), siMOF (red), and siKANSL1 (blue) treated cells using Seahorse XFe96 analyzer. O, Oligomycin; F, Carbonylcyanide-4-(trifluoromethoxy) phenylhydrazone (FCCP); R+A, Rotenone and Antimycin A. Right, basal and ATP-linked oxygen-consumption rate (OCR) was calculated. Mann-Whitney U test, *** $p < 0.0001$. Data represent mean \pm SEM; $n = 14$ –20 per sample.

(K) Coupling efficiency and respiratory control ratio were determined from respiratory curve. Data represent mean \pm SEM; $n = 14$ –20 per sample. Mann-Whitney U test, *p* value mentioned in figure. See also [Figure S4A](#).

RNA-sequencing (RNA-seq) strategy was based on poly-A enrichment, we were unable to enrich for all mtDNA-transcribed mRNAs (MT-mRNAs). Therefore, we performed qRT-PCR to study MT-mRNA levels after MOF depletion in glucose and galactose media. Consistent with RNA-seq data, mtDNA genes were globally downregulated in siMOF galactose (Figure 2F) and remained unaffected in siMOF glucose (data not shown). Furthermore, siMOF cells showed no significant change in levels of key mitochondrial regulatory factors like *POLRMT*, *TFAM*, or *MTPAP* and only a slight decrease in *MTERF* and *NRF1* levels (Figure 2F), a fact corroborating with siMOF-galactose RNA-seq data. We also observed a comparable global downregulation of mtDNA transcripts levels in KANSL1 (representative NSL member)-depleted cells (Figure 2G). Notably, we could exclude the possibility that altered mtDNA contents affect transcription levels in siMOF and siKANSL1 samples (Figure 2H). Taken together, these data show that MOF directly regulates expression of OXPHOS genes of both nuclear and mtDNA.

Next, we assessed the impact of MOF/KANSL1 loss on mitochondrial translation. Blue native electrophoresis showed reduced formation of respiratory supercomplexes in MOF- and KANSL1-depleted cells (Figure S3C). In vitro translation assays with freshly isolated mitochondria from siMOF and siKANSL1 samples (galactose) revealed reduced mitochondrial polypeptide synthesis (Figure S3D). Steady-state levels of nuclear-encoded OXPHOS subunits/regulators remained largely unaffected (Figures S3E and S3F).

Loss of MOF and KANSL1 Leads to Impaired Mitochondrial Respiration and Reduced MT-RNA Synthesis

To assess the functional impact of MOF/KANSL1 loss on mitochondria, we first evaluated the overall fitness of the organelle by scrutinizing its membrane potential in galactose. siMOF/siKANSL1 samples showed significant membrane depolarization (Figures 2I and S3G), a strong indicator of mitochondrial dysfunction. In light of OXPHOS gene deregulation, it was highly likely that the electron transport chain was impaired. We thus performed in vivo cellular respirometry assay using the Seahorse XF96e flux analyzer on HeLa cells. When comparing the respiration profiles of siSCRAM control with siMOF/siKANSL1 cells, we observed reduced respiration in the knockdown cells. Appropriate drug sensitivity implies that individual complexes are still

functional, albeit with lowered efficiency (Figure 2J). Basal, as well as ATP-linked, respirations were significantly reduced in the knockdown samples, but there was no difference in respiratory coupling efficiency or the respiratory control ratio between control and knockdown cells (Figure 2K). Incidentally, these phenotypes were observable also in glucose conditions (data not shown). siMOF cells did not show any significant defect in the major fuel-consumption pattern (Figure S4A), dismissing flawed nutrient utilization as a trigger for observed defects. In conclusion, depletion of MOF/KANSL1 reduces mitochondrial respiration.

Steady-state RNA levels are a reflection of two antagonistic processes: RNA synthesis and decay. Hence, reduced MT-mRNA levels of siMOF/siKANSL1 samples might be due to impaired RNA synthesis and/or increased turnover. To distinguish between the two, we labeled nascent RNA with 5-ethynyl uridine (EU) to monitor the dynamics of RNA synthesis and turnover in MOF/KANSL1 depleted cells (Figures 3A and 3B, see STAR Methods). Cytoplasmic 18S rRNA was considered a control. We observed that loss of MOF/KANSL1 impairs synthesis of MT-RNAs (*CYTB*, *ND5*, and *12S rRNA*) without affecting their stability (Figures 3A and 3B). Global levels of major mtDNA transcriptional and replication regulators remained unaffected in siMOF cells (Figures 3C and S3F). Thus, MT-RNA synthesis is impaired in the absence of MOF/KANSL1, resulting in reduced MT-RNA levels.

MOF and KANSL3 Bind mtDNA

The transcriptional data raised the possibility that MOF might affect the function or recruitment of mitochondrial proteins on mtDNA. To test this hypothesis, we developed in organello mtDNA immunoprecipitation (mtDIP) technique (see STAR Methods) for identifying mtDNA binding factors. We performed mtDIP to probe for mtDNA binding of transcription (*POLRMT*, *TFB2M*, and *MTPAP*) and replication (*POLG* and *SSBP*) factors (Figure 3D and 3E) in siMOF cells. The data were normalized to *TFAM*, an integral component of mitochondrial nucleoids. The distribution of *TFAM* itself was tested with multiple probes encompassing the mtDNA (Figures S4B–S4D). Previously, we had identified KANSL3 in the mitochondrial matrix. As it often functions in cooperation with MOF, we performed parallel experiments in KANSL3 knockdown background. We observed that MOF and KANSL3 depletion had no effect on the recruitment

Figure 3. MOF and KANSL1 Depletion Triggers Reduced MT-RNA Synthesis

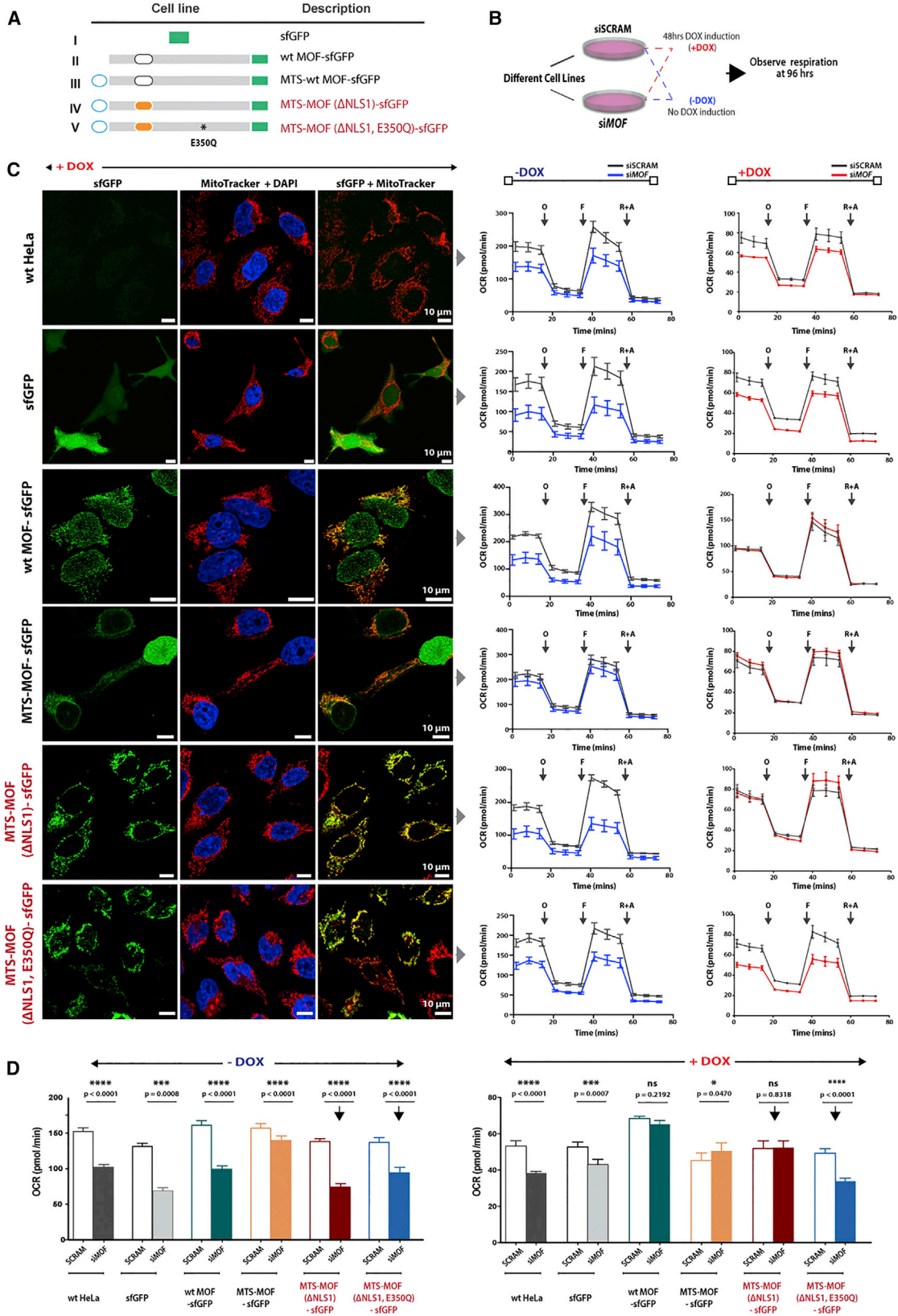
(A and B) Dynamics of RNA synthesis (A) and decay (B) calculated for siSCRAM control cells (black) and siMOF (red)- and siKANSL1 (blue)-treated cells in galactose media. Cartoons of the experimental schemes are shown on left. MT-RNAs are prefixed by MT. Data represent mean \pm SD of three biological replicates.

(C) Immunoblotting for mitochondrial transcription (*TFAM*, *POLRMT*, and *MTPAP*) and replication (*POLG* and *SSBP*) factors in galactose adapted siSCRAM and siMOF samples. Triangles denote specific bands.

(D and E) mtDIP assay performed in SCRAM control (white), siMOF (red), and siKANSL3 (yellow) cells for assessing *POLRMT* (two different antibodies used, A and B), *TFB2M*, *MTPAP*, *POLG*, and *SSB* binding to mtDNA. *TFAM* binding profile was used for normalization. Parallel experiments were performed in glucose (D) and galactose (E) media. Data represent mean \pm SEM of three biological replicates. See also Figures S4B–S4G.

(F) Realignment of mouse embryonic stem cell (mESC) ChIP-seq datasets (from Chelwicki et al., 2014) of mMOF (red), mKANSL3 (green), and mMCRS1 (orange) to mouse mtDNA (outer gray circle). NCR, non-coding region.

(G–I) mtDIP assay performed for MOF binding to mtDNA. Cartoon shows NCR of human mtDNA with aligned primers. (G) mtDIP-qPCRs were performed in control (siSCRAM, white) and siMOF (H)/siKANSL3 (I) cells. Primers effectively span the entire mtDNA. Down arrows indicate the regions consistently showing highest enrichments in all experiments. TAS, transcription-associated site; HVS1/2, hyper variable site 1/2; LSP, light strand promoter; HSP1/2, heavy strand promoter 1/2. Data represent mean \pm SEM of three biological replicates. See also Figures S4H, S4I, S5A, and S5B.



(legend on next page)

of any of the interrogated factors in glucose medium (where we also did not observe a transcriptional defect upon MOF loss) (Figure 3D). Strikingly, in galactose media, we observed accumulation of signal of mtDNA transcription regulators, POLRMT, TFB2M, and MTPAP, but not components of the replication machinery (Figure 3E). Interestingly, chemically impaired mtDNA transcription leads to similar accumulation of transcription factors (Figures S4E–S4G), indicating that transcription is compromised upon loss of MOF/KANSL3 (also see Discussion).

These results, coupled with known DNA-binding properties of MOF/KANSL3, raised the interesting possibility of MOF and KANSL3 associating with mtDNA. High-functional conservation of NSLs prompted us to first check for mtDNA binding in published mouse ESC ChIP-seq profiles of MOF, KANSL3, and MCRS1 (Chelmicki et al., 2014). We focused on mtDNA-specific reads, which were filtered out in original analyses. MOF and KANSL3, but not MCRS1, signals were enriched on the non-coding region (NCR) of mouse mtDNA (Figure 3F). Consistently, human MOF/KANSL3 mtDIP signals were maximally enriched on the NCR of human mtDNA (Figures 3H and S4H). Incidentally, this region is associated with regulation of mtDNA transcription and replication (Mercer et al., 2011). Signal specificity was verified by its sensitivity to MOF/KANSL3 depletion. Though the MOF/KANSL3 binding mirror each other, only MOF shows dependency on KANSL3 and not vice versa (Figures S3I and S4I), resonant of their co-occupied nuclear targets (Chelmicki et al., 2014). Finally, we visualized MOF-mtDNA association by 3D HR-SIM (Figures S5A and S5B). The speckled pattern of the MOF-sfGFP signals was similar to that observed before for endogenous MOF (Figure 1A). In conclusion, MOF and KANSL3 associate with mtDNA in both human and mouse cells.

Mitochondrial Pool of MOF Can Rescue Respiratory Defects

To study the contribution of mitochondrial pool of MOF more concretely in respiration, we generated various sfGFP-tagged MOF-derivative (inducible) cell lines (Figure 4A). Particularly, we enforced MOF transport to mitochondrial matrix by fusing a synthetic COX4A MTS (referred to as MTS from here on) at its N terminus. Unfortunately, the MTS was insufficient to fully restrict WT MOF to mitochondria, so we generated additional cell lines with mutated NLS1 (Δ NLS1; mentioned in Figure 1H) (Figure 4A, IV and V). A catalytic mutant (E350Q) version of MTS-MOF(Δ NLS1) was also generated.

We first verified doxycycline (DOX)-induced protein expression for all cell lines (Figures S5C and S5D). Then, parallel

MOF/SCRAM knockdowns were performed in different cell lines, followed by respirometry study (Figure 4B, see STAR Methods). In the Figure 4C immunofluorescence panel, we present the intracellular distribution pattern of every cell line in a separate row. Adjacent to them, the respiratory profiles of respective lines are shown, both with and without DOX induction (Figure 4C, respiratory curves). Following siMOF treatment, all cell lines showed significant reduction in basal respiration (Figure 4D, left graph), indicating their inherent response to MOF depletion. DOX-induced transgene expression (Figure 4D, right graph) led to the following important conclusions: (1) respiratory defects were not rescued by simple application of DOX or sfGFP expression in control cell lines (wtHeLa and sfGFP); (2) ectopic expression of MOF rescued basal respiration, indicating that the respiratory defects are a direct consequence of MOF loss; (3) mitochondrial pool of MOF is sufficient to rescue the phenotype; (4) finally, the mitochondrial pool of catalytic mutant (E350Q) MOF could not rescue the respiratory defects. A similar outcome was recorded for respirometry studies on glucose-adapted cell lines (Figure S5E). Taken together, these data provide strong evidence for a functional significance of MOF in mitochondria and the need for its enzymatic activity in mitochondrial respiration.

Mitochondrial Pool of MOF Can Rescue mtDNA Transcriptional Defects

We next wanted to investigate the role of mitochondrial MOF in mtDNA transcription. Accordingly, we adopted a rescue strategy like the one used before (Figures 5A and 5B). Following MOF loss (and DOX induction), MT-mRNA levels were restored in wtMOF-expressing cells (Figure 5C), implying a direct role of MOF in mtDNA transcription. At this point, it is important to consider two possible scenarios. First, nuclear and mitochondrial MOF may either work independently or cooperatively to regulate MT-RNA levels. In the latter case, mitochondrial MOF would at best only show partial rescue. Second, in spite of common polycistronic origin, individual MT-mRNAs are differentially regulated (Mercer et al., 2011). It is thus possible that distinct pools of MOF may vary in their influence on different MT-mRNAs. Importantly, these two scenarios are not mutually exclusive.

To assess the impact of mitochondrial MOF, catalytically active and mutated versions of MOF: MTS-MOF(Δ NLS1)-sfGFP and MTS-MOF(Δ NLS1, E350Q)-sfGFP, respectively, were used in further studies (Figure 5B). As shown in Figure 5D, both MOF derivative lines show similar expression levels after DOX induction, making them suitable for comparison. Interestingly, the cells regulate the levels of the ectopically expressed MOF

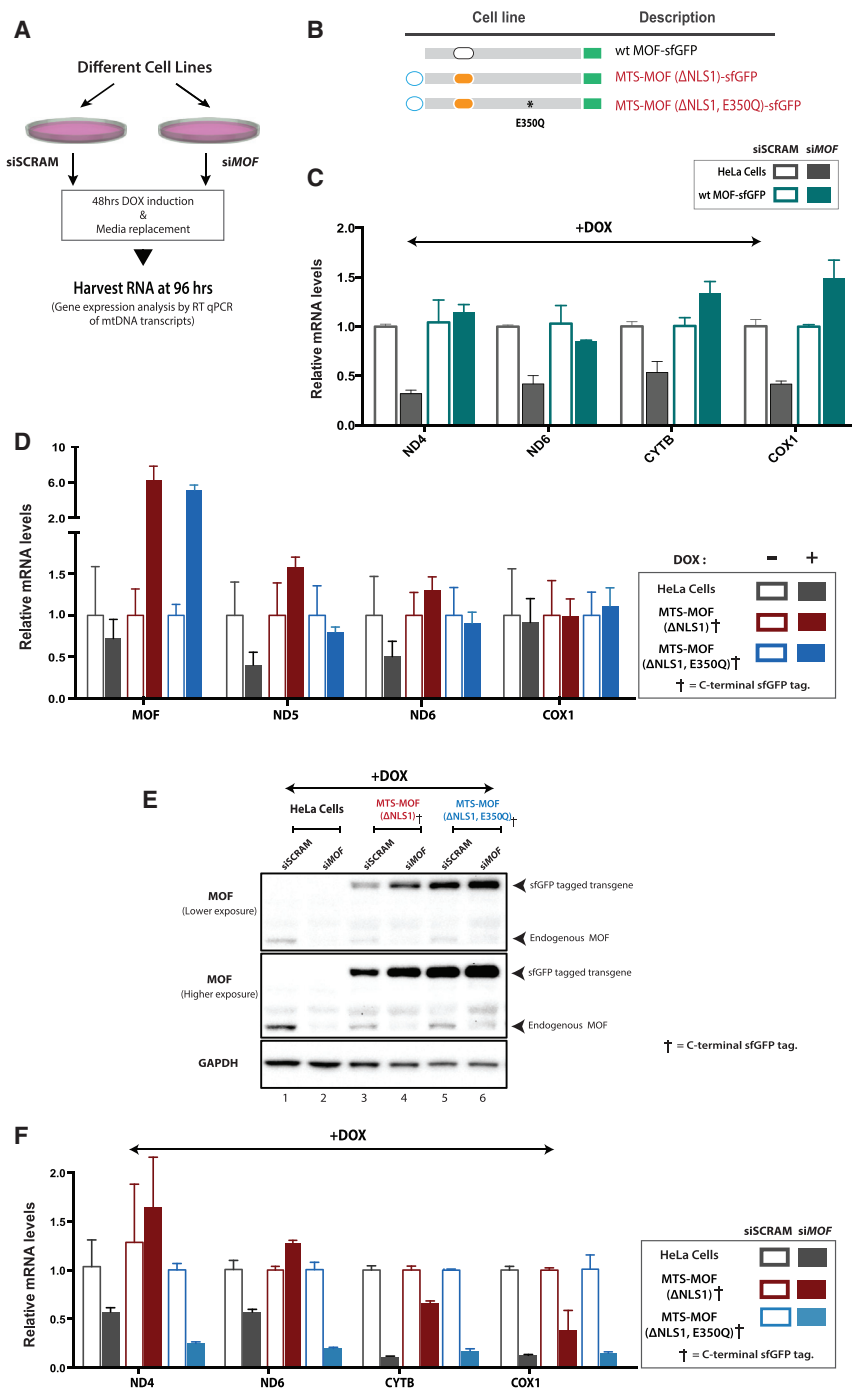
Figure 4. Mitochondrial Pool of Catalytically Active MOF Can Rescue Respiratory Defects

(A and B) Schematic illustrations of the doxycycline (DOX)-inducible cell lines used in rescue experiments (A). Features represented: COXIV MTS (blue ellipse); MOF (gray thick line); MOF's nuclear localization signal 1 (NLS1, black ellipse) and its mutated form (Δ NLS1, orange filled ellipse); sfGFP (green filled rectangle); asterisks indicate point mutation (E350Q) in MOF's HAT domain. (B) Experimental scheme used for rescue of mitochondrial respiratory defects (triggered by MOF loss) in cell lines.

(C) Left, immunofluorescence images of the cell lines, co-stained with MitoTracker. Right, bioenergetic profiles of cells following siSCRAM or siMOF treatment are shown. Two respiratory traces are shown either with or without DOX-induced transgene expression. Each row shows a different cell line. Mitochondrially restricted MOF cell lines are denoted in red. Data represent mean \pm SEM of four or five biological replicates. O, oligomycin; F, FCCP; R+A, Rotenone + Antimycin A.

(D) Basal respiration calculated for all cell lines after siSCRAM and siMOF treatment, with or without DOX induction. Data represent mean \pm SEM of four or five biological replicates. Ordinary one-way ANOVA, p values shown in figure.

See also Figures S5C–S5E.



derivative based on the presence or absence of the endogenous protein (Figure 5E). This difference was more prominent in cells expressing the KAT-active version of the protein compared to the E350Q (Figure 5E, MOF lower exposure, lanes 3 and 4 versus lanes 5 and 6).

Transcriptional rescue experiments revealed that *ND4* and *ND6* mRNAs are rescued by mitochondrial MOF, but not its catalytic mutant version (Figure 5F). These proteins are critical for functional assembly of the respiratory complex I

on some mtDNA transcripts. Thus, the mitochondrial pool of MOF is sufficient to rescue mtDNA levels, and this function is reliant on its KAT activity.

Mof Deletion in Murine Hearts Causes Acute Cardiomyopathy

Based on the in vitro observations of mitochondrial defects in *Mof*-depleted cells, we wanted to analyze the effects of *Mof* ablation in vivo. Constitutive *Mof* deletion is embryonically lethal

Figure 5. Mitochondrial Pool of Catalytically Active MOF Can Restore mtDNA Transcript Levels

(A) Experimental strategy adopted for rescue of mtDNA transcriptional defects triggered by MOF loss in different cell lines (galactose media).

(B) Cartoon of the cell lines used in the rescue assay. For details, see Figure 4A legend.

(C) Rescue of mtDNA transcription by MOF. Each cell line was treated with siSCRAM and siMOF, followed by DOX induction. Gray, HeLa cells; teal, WT MOF-sfGFP cell line. Data represent mean \pm SEM of three biological replicates.

(D) qRT-PCR for different mRNA levels before (hollow bars) and after (filled bars) DOX induction in various cell lines. Gray, HeLa cells; red, MTS-MOF(Δ NLS1)-sfGFP; blue, MTS-MOF(Δ NLS1, E350Q)-sfGFP. Data represent mean \pm SEM of three biological replicates. Experiments were performed in galactose growth media without any siRNA treatment.

(E) Western blots showing effect of siMOF treatment and DOX induction on endogenous MOF levels in WT HeLa, MTS-MOF(Δ NLS1)-sfGFP, and MTS-MOF(Δ NLS1, E350Q)-sfGFP cell lines. Arrowheads show the endogenous MOF band and its tagged version.

(F) Same experimental setup as Figure 5C, but the following cell lines were used instead: mitochondrially tethered MOF (MTS-MOF(Δ NLS1)-sfGFP, red) and its catalytic inactive counterpart (MTS-MOF(Δ NLS1, E350Q)-sfGFP, blue). HeLa control cells are in gray. Data represent mean \pm SEM of three biological replicates.

with single-point mutations leading to pathological outcomes (Perales-Clemente et al., 2010; Kirches, 2011). Incidentally, a previous study had demonstrated that cells with a mutated *ND6* gene show reduced OXPHOS and fail to grow in galactose media (Bai and Attardi, 1998). Thus, downregulation of *ND4* and *ND6* will clearly compromise mitochondrial function.

Additionally, we observed partial rescue of *CYTB* and *COX1* mRNAs by catalytically active mitochondrial MOF and not its mutant counterpart (Figure 5F). These data indicate a cooperative role of two pools of MOF (nuclear and mitochondrial)

in mice (Gupta et al., 2008; Thomas et al., 2008). Therefore, using muscle creatine kinase (MCK or *Ckm*)-driven Cre (Brüning et al., 1998), we generated cardiac- and skeletal-muscle-specific conditional *Mof* knockout (KO) mice. The *Ckm* promoter expression starts from E13 (Lyons et al., 1991) and is highly limited to cardiomyocytes and skeletal muscles, reaching maximal levels by P10 (Trask and Billadello, 1990). *Mof* KO mice show Mendelian distribution and develop normally with no apparent morphological defects during the first week after birth. However, their behavior changed dramatically from P10 onward; they displayed decreased spontaneity, extreme frailty, physical inactivity, and high sensitivity to even minor stress conditions, with several KO mice dying unexpectedly during handling. Most KO mice died within P16–P23, with peak mortality around P17.

Mof deletion (Figures S6A and S6B) led to loss of H4K16ac staining in cardiomyocytes, widely observed from P10 and complete by P16 (Figure 6A), coinciding with the onset of the cardiac phenotype. Post-mortem examination revealed that the mutant mouse hearts displayed signs of hypertrophy, with cardiac dilation (Figure 6B), higher heart-to-body-weight ratio (Figure 6C), and an increased cardiomyocyte cross-sectional area (Figures 6E and S6C). In parallel, progressive accumulation of interstitial fibroblasts and collagen fibers was observed in KO hearts (Figures 6D and S6D). Remodeling of the extracellular matrix was accompanied by elevated levels of connective tissue growth factor (*Ctgf*) and periostin (*Postn*) mRNA in mutant hearts (Figure S6E).

Cardiomyocytes in neonatal mice undergo karyokinesis without cytokinesis (acytokinetic mitosis), forming binucleated cells up to P10 (Soonpaa et al., 1996). As MOF is known to be involved in cell-cycle regulation (Taipale et al., 2005), we checked for the relative cardiomyocyte nuclei content in KO hearts from postnatal day 5–9 and found no difference from the control animals (Figure S6F). Hence, cardiomyocyte proliferation is normal in KO hearts. Echocardiography of KO hearts showed strongly decreased cardiac function with left ventricular dilation (Figures S7A and S7B and Movie S1).

Mitochondrial Degeneration Follows *Mof* Deletion, Causing Loss of Myocytes in Heart and Spindle Fibers in Skeletal Muscles

Mof-deleted hearts show rapid deterioration in health, with cardiac failure by P17. We reasoned that the days preceding death would provide valuable insight into the pathophysiology of phenotype. Consequently, we performed electron microscopic (EM) analysis on cardiac sections of P15 KO and control *Mof*^{+/+} and *Mof*^{+/-} mice. While the control hearts looked normal (Figure 6F, top), sections from KO hearts displayed a wide spectrum of mitochondrial alterations. The severity of the phenotype ranged from regions with no observable defects to heavily degenerated cells. We noted a general trend of overall increase in lipid droplet (LD) deposition, even in otherwise-intact regions (Figure 6F, I). Often, cardiomyocytes showed a mixture of normal and dysfunctional (swollen) mitochondria with intermittent glycogen deposition (Figure 6F, II). At the other end of the spectrum, we noted mitochondria at various stages of degeneration (Figure 6F, III and IV).

Mitochondria are the major source of reactive oxygen species (ROS) in the heart. Hence, we used ROS deposition as a readout of mitochondrial dysfunction. KO heart sections showed significant ($p < 0.001$) increase in dihydroethidium (DHE, an indicator of ROS) levels, starting from as early as P10 (Figure 6G).

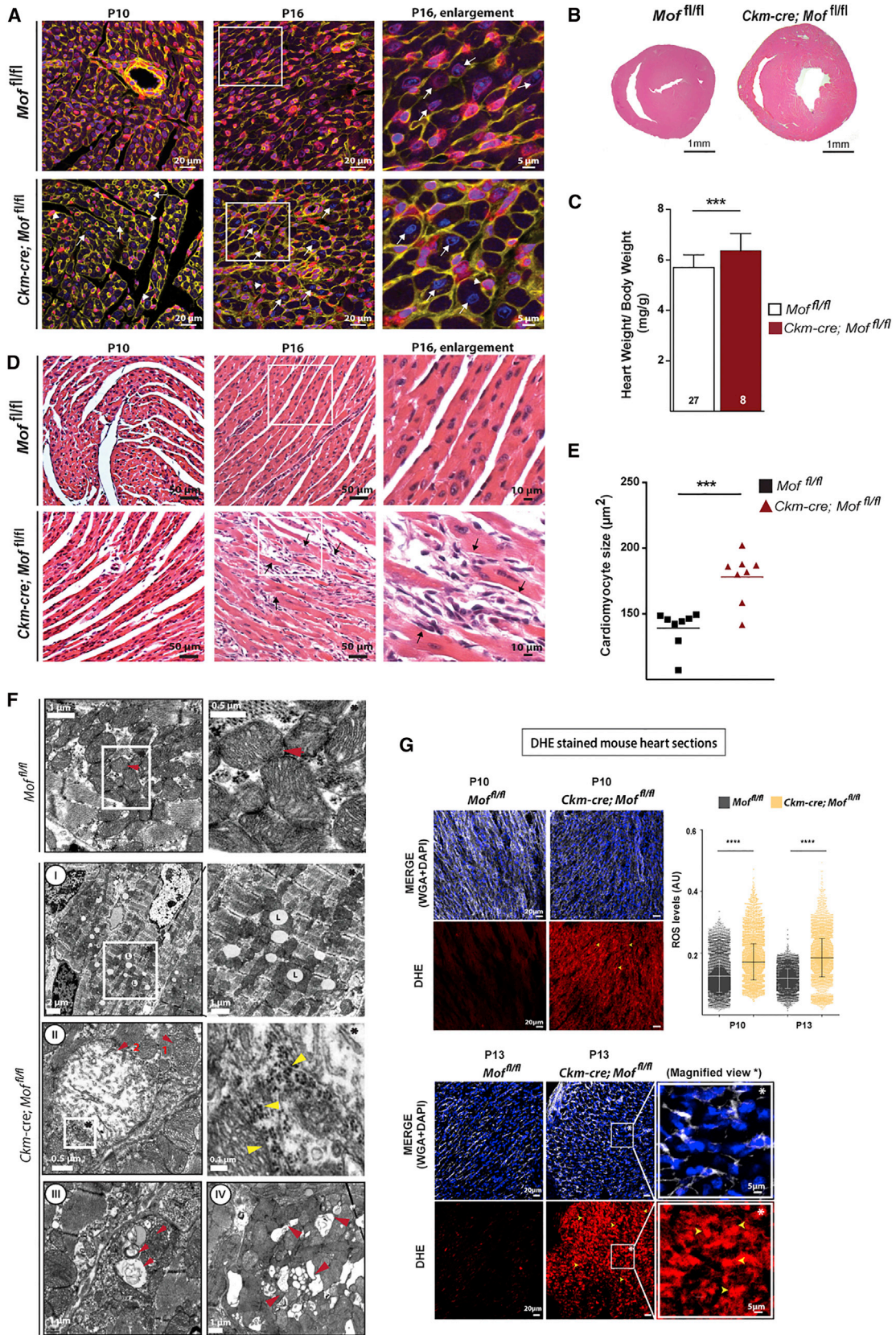
The *Ckm* Cre is also active in skeletal muscles. However, there was no gross morphological defect in the skeletal tissues of the KO mice (data not shown). EM analysis of skeletal muscle (hind limb) sections (control tissues, Figure S7C, top) from P15 mice mostly showed mild to no alterations in mitochondrial morphology (Figures S7C and S7I) except a specialized tissue region known as the spindle fibers or muscle spindles (Figure S7C, II), which presented severe mitochondrial degeneration, evocative of cardiomyocyte sections (Figure 6F). These intrafusal fibers are embedded within the typical (extrafusal) muscle fibers and remain continuously active to maintain muscle tone. Surprisingly, we noted significant ($p < 0.001$) elevation of ROS levels (Figure S7D) in skeletal sections of P13 KO mice. These data suggest that loss of MOF can have variable impact on mitochondria of different cell types in the same organ, correlating with the usage of organelle. In conclusion, loss of MOF causes mitochondrial dysfunction, which is aggravated by high usage of the organelle.

Mitochondrial Pathways Are Downregulated in *Mof*-Deleted Cardiomyocytes

What triggers the rapid cardiomyopathy of *Mof*-deleted hearts? To gain a molecular insight into this question, we performed RNA-seq analysis on P15 cardiomyocytes. Briefly, nuclei isolated from control and KO P15 mice hearts were sorted by FACS to obtain pure cardiomyocyte nuclei for RNA-sequencing (Figure 7A). Gene set enrichment analysis (GSEA) of differentially expressed genes (FDR < 0.05) was performed to identify significantly affected pathways (Figure 7B). Strikingly, a bulk (8/11) of the downregulated pathways transpire in mitochondria, essentially affecting energy production (oxidative phosphorylation) and nutrient (lipid or amino acid) metabolism. Of the upregulated pathways, transcriptional activation of signaling cascades associated with hypertrophy (NF- κ B, MYC signaling etc.), fibrosis (focal adhesion, collagen formation), or cardiomyocyte degeneration (apoptosis, p53 signaling) was seen. These findings are consistent with the phenotype of progressive cardiac myopathy.

To filter out the primary effects of *Mof* KO, we used previously generated (mESC) MOF ChIP-seq data (Chelmicki et al., 2014) and identified MOF-bound (differentially expressed) targets to be used in subsequent analysis. We first focused on mitochondrial genes, since mitochondrial dysfunction was implicit from GSEA. We found that 42% (608/1432) of these genes are bound by MOF (Figure 7C, I). Of the later gene set, the affected subset (184) showed both upregulation and downregulation (Figure 7C, II) of expression. Interestingly, a closer inspection of the associated mitochondrial pathways revealed a similar trend as observed before with GSEA (Figure 7C, III). It is thus implicit that affected genes coding for mitochondrial proteins are mostly under direct regulation of MOF.

Next, we examined the major regulatory networks affected by *Mof* deletion. Using an MOF-bound gene list, we performed causal network analysis (in IPA) for identifying gene clusters



(legend on next page)

co-regulated by a master regulator (Figure 7D). Based on the trends of individual genes of the network, Z scores for pathway activation or inhibition (positive or negative, respectively) were determined. In many cases, the master regulator itself remained unaffected. We observed activation of MAP4K4, as well as FGFR1 network, both associated with hypertrophic cardiac remodeling. Additionally, a major oxidative stress response pathway, NRF2, was also activated. On the other hand, mTORC2/RICTOR (important for cardiac structure maintenance and mechanical stress response), PPARA (critical for myocardial energy and lipid metabolism), and KLF15 (negative regulator of myocardial hypertrophy) were moderately deactivated. It is noteworthy that the implicated networks remained significant even when the entire dataset (with all differentially expressed genes) was considered. Consistent with the phenotypic data, hypertrophic signaling emerged as a prime outcome of *Mof* deletion at the molecular level. Lastly, network analysis (see STAR Methods) of the beta-oxidation pathway revealed that relatively few molecules (9/84) were affected in the represented gene set (Figure 7E, left). Yet, this led to predicted inhibition of the PPAR (PPARA, PPARD, and PPARGC1) master regulatory network and effectively the pathway. Similarly, we also generated a common network map for the mitogen-activated protein (MAP) kinases involved in cardiac functionality (Figure 7E, right). We observed Ras-complex upregulation, which had a positive regulatory effect on the entire MAPK network. In summary, the molecular effect of *Mof* deletion could be broadly classified into two groups: (1) induction of networks triggering cardiac remodeling (hypertrophy) and (2) defects in lipid-based energy metabolism.

DISCUSSION

In this study, we report the presence of a functional pool of the nuclear lysine acetyl transferase MOF in mitochondria. We identified bona fide MTS in two NSL members (KANSL2 and KANSL3). MOF and KANSL1 showed mitochondrial localization, but no clear MTS was detected in them. It might be that MOF/KANSL1 have cryptic internal targeting signal, as seen in CREB, p53, yeast BCS1 protein, HSP10, and ISD11 (Leigh-Brown et al., 2010; Vögtle et al., 2009). Alternatively, KANSL2/KANSL3 or mitochondrial chaperones may facilitate their transport to mitochondria.

Interestingly, we noted two populations of MOF in mitochondria: in the inner matrix and at the outer membrane. The latter can simply be an uncleaved version of the protein. But it can also be a functional isoform or a post-translationally modified version of MOF. Future work into mitochondrial targeting and dynamics of these proteins would help in understanding their function in the organelle.

In the absence of MOF/KANSL1, MT-RNA synthesis is reduced, while RNA stability remains unaffected, resulting in reduced (steady-state) levels of the MT-RNAs. Mitochondrial translation is also impaired. The physiological outcome is mitochondrial depolarization and compromised respiration. Consistently, RNA-seq analysis of *siMOF* (galactose) cells revealed mitochondrial dysfunction and OXPHOS deregulation. MOF/KANSL3 depletion (galactose) causes increased accumulation of critical mitochondrial transcription factors like POLRMT, TFB2M, and MTPAP (Bestwick and Shadel, 2013) on mtDNA. The replication factors (POLG and SSBP) were not affected. Thus, mitochondrial transcription machinery assembly on mtDNA is sensitive to MOF/KANSL3 levels. We speculate that, in the absence of MOF/KANSL3, the mitochondrial transcription factors are blocked or “stuck” and cannot be efficiently released from DNA. MOF/KANSLs may either physically interact with or facilitate post-translational modification of members of the transcription machinery. Alternatively, MOF may act by some other as-yet-unknown means.

A mitochondrial pool of MOF was sufficient to rescue respiratory and transcriptional defects (triggered by *Mof* loss). Importantly, a catalytic mutant (E350Q) version of the same was unable to rescue the phenotypes, suggesting a functional importance of the MOF’s enzymatic activity in mitochondria. This provides the first step toward understanding the importance of MOF’s enzymatic activity in mitochondrial function. In the future, it will be important to address how MOF’s enzymatic activity is involved in mitochondrial homeostasis.

MOF shows remarkable functional plasticity by association with different proteins. While MOF/MSL complex selectively acetylates H4K16, MOF/KANSL complex shows broader substrate specificity and acetylates histone H4 on K5, K8, K12, and K16 residues on reconstituted nucleosomes (Figures S7E and S7F). Therefore, it is highly likely that the mitochondrial

Figure 6. *Mof*-Deleted Mouse Hearts Show Mitochondrial Degeneration and Cardiac Failure

(A–G) Cardiac phenotyping of *Mof*^{fl/fl} (Control) and *Mof*^{fl/fl}; *Ckm-cre* (KO) mice.

(A) Sections of control and KO mouse hearts from P10 and P16 animals. Cell membrane is stained with wheat germ agglutinin (WGA, yellow), and the nucleus is stained with DAPI (blue) along with anti-H4K16ac (magenta). The enclosed area within P16 image panel is shown at a higher magnification on its right. White arrowheads denote DAPI-stained cardiomyocyte nuclei, positive or negative for H4K16ac staining.

(B) H&E-stained transverse sections of ventricles from P16 control and KO mice.

(C) Heart-to-body-weight ratios of P16 control (white bars, n = 27) and KO mice (red bars, n = 8). Error, ± SEM. Unpaired *t* test, ***p = 0.0051.

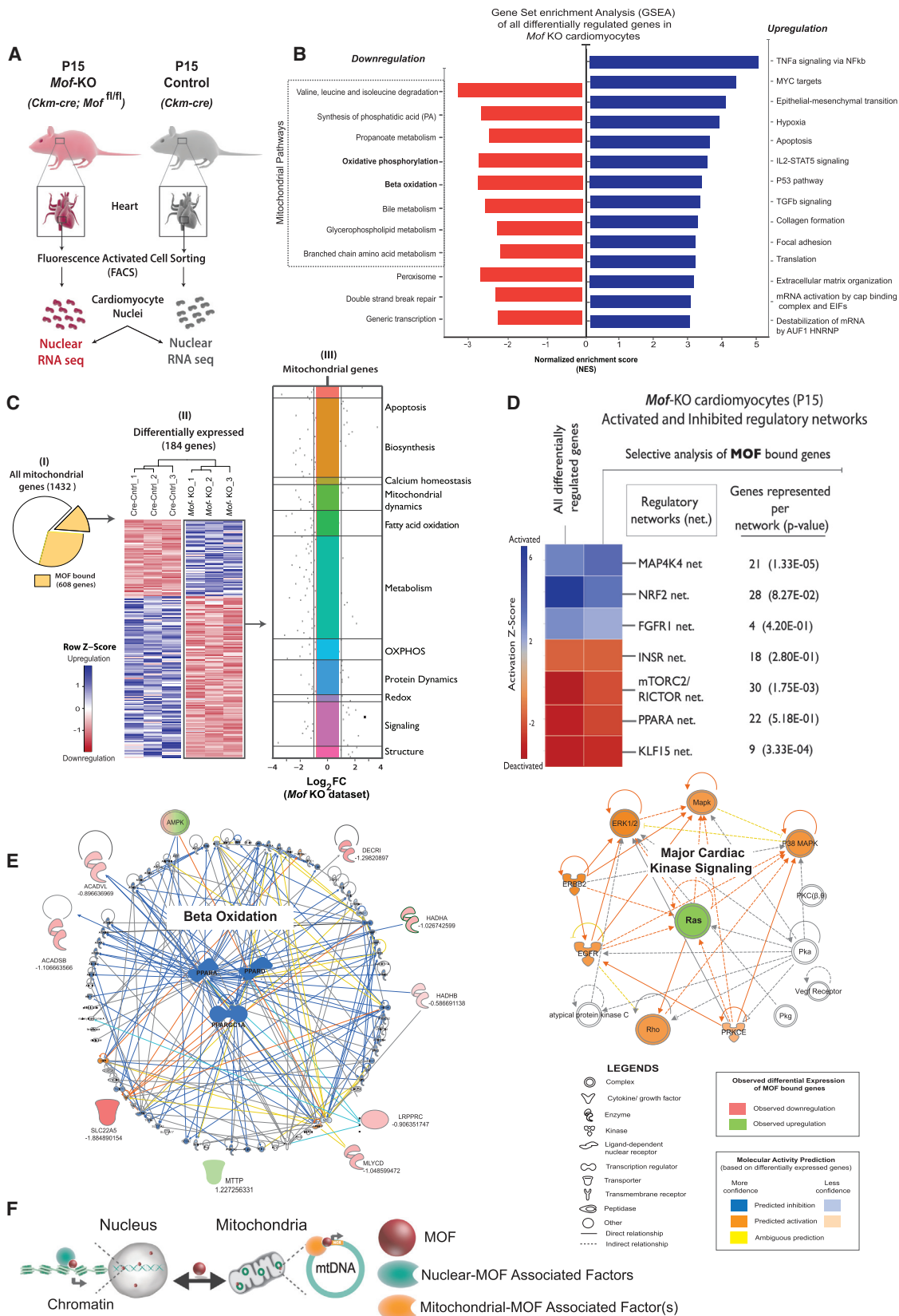
(D) H&E staining of heart sections to observe cardiac cytoarchitecture of (P10 and P16) control and KO mice. Black arrows, regions with cardiomyocyte disarray.

(E) Mean cardiomyocyte cross sectional area of P16 control (black squares, n = 8) and KO (red triangles, n = 8) animals, determined from wheat gram agglutinin (WGA) staining. Unpaired *t* test, ***p < 0.005.

(F) Electron micrograph of cardiac sections from P15 control (n = 5) and KO (n = 4) mice. Top panel shows control heart tissues. The ranges of phenotypes observed in KO hearts are shown below. (I) Regions with elevated lipid droplet (L) accumulation. (II) A cardiomyocyte with both healthy (1) and swollen mitochondria (2). (III and IV) Some regions showed mitochondria at different stages of degeneration. Magnified views of boxed regions are shown on right of respective images. Red triangles, mitochondria; yellow triangles, glycogen; L, lipid droplet. See also: Figure S7C.

(G) DHE staining of control and KO heart sections. Data were collected from P10 and P13 mice (n = 3). Mean fluorescence signals were calculated from multiple images of each sample set and represented as relative ROS level in scatterplot. Yellow triangles, ROS accumulation. Unpaired *t* test, ***p < 0.005. See also, Figure S7D.

See also, Figures S6A–S6F, S7A, S7B, and Movie S1.



(legend on next page)

pool of MOF and KANSL proteins have additional functions and possibly new acetylation targets. We can extrapolate from their functions to predict critical roles of MOF/KANSLs or their signatory acetylation marks in other cell types with high-energy demands, such as neurons (Rugarli and Langer, 2012). Interestingly, transient upregulation of H4K12ac is essential for hippocampus-based learning, and its misregulation is implicated in age-related memory impairment in Alzheimer models (Plagg et al., 2015). Additionally, a striking example is provided by the *KANSL1* haploinsufficiency syndrome, called Koolen-de Vries (or 17q21.31 microdeletion) syndrome (Koolen et al., 2012). The key features of this disorder, namely neurological/developmental impairments, multi-organ dysfunction, tissue heterogeneity, and variable severity, are also classical hallmarks of mitochondrial diseases. In fact, all of these symptoms are variably displayed in a constellation of mitochondrial disorders.

In our current work, using cardiac and skeletal tissue models, we reveal that, following *Mof* depletion, there is variability in clinical presentation of phenotypes across different tissues, correlating with its energy consumption. Mouse cardiomyocytes are packed with mitochondria (~37%) and occupy 75% of the heart's volume (Barth et al., 1992), making them highly reliant on mitochondrial energy synthesis. While the heart is primarily aerobic and has one of the highest metabolic rates (~440 kcal/kg/day), skeletal muscle is chiefly glycolytic and has low resting metabolic rates (~13 kcal/kg/day) (Wang et al., 2010). The divergent phenotype(s) observed in the two organs provide a great insight into the role of MOF in mitochondrial respiration. This is supported by recent reports of downregulation of MOF in failing human and murine hearts (Qiao et al., 2014). However, how the nuclear and mitochondrial pools of MOF contribute to regulation of transcription and energy metabolism in complex tissues will be an important avenue for future studies.

In conclusion, the presence of MOF and KANSL proteins in mitochondria sheds new light into functioning of this versatile complex in contextual gene regulation. We propose the MOF and KANSL proteins may serve a sensory function to coordinate gene expression in both the nucleus and mitochondria based on the cellular metabolic status (Figure 7F). We expect that future work on the function of these proteins can contribute to understanding the dynamics of environment-induced epigenetic changes in cellular functions.

STAR★METHODS

Detailed methods are provided in the online version of this paper and include the following:

- KEY RESOURCES TABLE
- CONTACT FOR REAGENT AND RESOURCE SHARING
- EXPERIMENTAL MODEL AND SUBJECT DETAILS
 - Mouse Strains
 - Plasmids and Cell Lines
- METHOD DETAILS
 - Cell Culture and Maintenance
 - Immunocytochemistry and confocal microscopy
 - Multi-color 3D high-resolution structured illumination microscopy (HR-SIM)
 - Prediction of mitochondrial targeting sequences
 - Prediction of nuclear localization signal (NLS)
 - Western blotting
 - Protein import into yeast mitochondria
 - Blue native electrophoresis
 - Cellular fractionation and knockdowns
 - Functional mitochondria isolation and purification
 - In organello translation in isolated human mitochondria
 - Proteinase K protection assay
 - Nucleic acid extraction and quantitative RT PCR
 - RNA decay and turnover experiment
 - Determination of mitochondrial membrane potential by JC-1 staining
 - Bioenergetic profiling of cells
 - mtDNA immunoprecipitation (mtDIP)
 - Ethidium bromide (EtBr) treatment
 - Data visualization of mouse ChIP-seq profiles
 - Rescue experiments
 - Experimental Optimization
 - RNA-seq experiment on HeLa cells and mouse cardiomyocytes
 - Echocardiography
 - Histology and immunohistochemistry
 - Ploidy analysis of cardiomyocyte nuclei
 - Dihydroethidium (DHE) staining for ROS detection
 - Electron microscopy
 - Histone acetyl transferase (HAT) assay
- QUANTIFICATION AND STATISTICAL ANALYSIS
- DATA AND SOFTWARE AVAILABILITY

Figure 7. RNA-Seq Analysis of *Mof*-Deleted Cardiomyocytes

(A) Schematic representation of the strategy adopted for isolation of P15 cardiomyocyte nuclei from *Mof^{fl/fl}* (Control) and *Mof^{fl/fl}; Ckm-cre* (KO) mice for RNA-seq analysis.

(B) GSEA of all differentially expressed genes in KO cardiomyocytes. Pathways ($p < 0.05$) are classified as upregulated (blue) or downregulated (red) based on their normalized enrichment scores (NES), presented in x axis.

(C) Pie chart representing all mouse mitochondrial genes (1,432), with yellow inset showing the genes bound by MOF (608) in mESC (from Chelmicki et al., 2014). Heat map represents the differentially expressed genes out of the bound ones.

(D) MOF-bound genes were extracted from the RNA-seq dataset and upstream regulator analysis was performed on differentially expressed genes. Heatmap showing affected gene networks that are bound by MOF (in mESC) and deregulated in KO dataset. Pathways are clustered by the Z scores for predicted activation (blue) or inhibition (red).

(E) Network maps were generated for critical pathways involved in cardiac function and RNA-seq dataset (for MOF-bound genes) was overlaid on them. The two major (affected) networks are displayed in the figure, namely beta-oxidation and kinase signaling.

(F) A working model depicting the role of MOF as a bi-organelle transcription regulator of OXPHOS genes in nucleus and mitochondria.

SUPPLEMENTAL INFORMATION

Supplemental Information includes seven figures, one table, and one movie and can be found with this article online at <http://dx.doi.org/10.1016/j.cell.2016.09.052>.

AUTHOR CONTRIBUTIONS

Conceptualization, A.C. and A.A.; Methodology, A.C.; Investigation, A.C., J.S., J.L., T.S., R.G., S.P., L.H., L.B., C.M., A.P., S.A., and O.K.; Analysis, A.C., A.H.S., and S.A.; Visualization, A.C. and A.H.S.; Writing, Original Draft, A.C. and A.A.; Writing, Review and Editing, A.C., A.A., L.H., N.P., and T.B.; Funding Acquisition, A.A.; Supervision, A.A.

ACKNOWLEDGMENTS

We are grateful to S. Taylor (University of Manchester) for providing HeLa Flp-In T-REx cells. We are thankful to M. Shvedunova and T. Chelmicki for their generous help in various experiments. We thank F. Duendar and T. Manke for bioinformatics support and T. Laemmermann and A. Rambold for critical reading of the manuscript. The MPIIE core facilities for Imaging, Deep sequencing, Mouse and FACS have been invaluable for this project. A.A. is supported by DFG funded SFB746, SFB992, SFB1140. A.A., N.P., L.H., and T.B. are part of the BIOS II excellence cluster. L.H., S.P., and R.G. were supported by the SFB992 and DFG HE 2073/5-1. T.B. and N.P. are supported by grants from the DFG (SFB746; BE 4679/2-1; PF 202/8-1).

Received: February 18, 2016

Revised: June 22, 2016

Accepted: September 27, 2016

Published: October 20, 2016

REFERENCES

- Akhtar, A., and Becker, P.B. (2000). Activation of transcription through histone H4 acetylation by MOF, an acetyltransferase essential for dosage compensation in *Drosophila*. *Mol. Cell* 5, 367–375.
- Backs, J., Song, K., Bezprozvannaya, S., Chang, S., and Olson, E.N. (2006). CaM kinase II selectively signals to histone deacetylase 4 during cardiomyocyte hypertrophy. *J. Clin. Invest.* 116, 1853–1864.
- Bai, Y., and Attardi, G. (1998). The mtDNA-encoded ND6 subunit of mitochondrial NADH dehydrogenase is essential for the assembly of the membrane arm and the respiratory function of the enzyme. *EMBO J.* 17, 4848–4858.
- Barth, E., Stämmler, G., Speiser, B., and Schaper, J. (1992). Ultrastructural quantitation of mitochondria and myofilaments in cardiac muscle from 10 different animal species including man. *J. Mol. Cell. Cardiol.* 24, 669–681.
- Becker, T., Wenz, L.S., Kruger, V., Lehmann, W., Muller, J.M., Goroncy, L., Zufall, N., Lithgow, T., Guiard, B., Chacinska, A., et al. (2011). The mitochondrial import protein Mim1 promotes biogenesis of multispanning outer membrane proteins. *J. Cell Biol.* 194, 387–395.
- Bestwick, M.L., and Shadel, G.S. (2013). Accessorizing the human mitochondrial transcription machinery. *Trends Biochem. Sci.* 38, 283–291.
- Brüning, J.C., Michael, M.D., Winnay, J.N., Hayashi, T., Hörsch, D., Accili, D., Goodyear, L.J., and Kahn, C.R. (1998). A muscle-specific insulin receptor knockout exhibits features of the metabolic syndrome of NIDDM without altering glucose tolerance. *Mol. Cell* 2, 559–569.
- Cai, Y., Jin, J., Swanson, S.K., Cole, M.D., Choi, S.H., Florens, L., Washburn, M.P., Conaway, J.W., and Conaway, R.C. (2010). Subunit composition and substrate specificity of a MOF-containing histone acetyltransferase distinct from the male-specific lethal (MSL) complex. *J. Biol. Chem.* 285, 4268–4272.
- Chelmicki, T., Dünder, F., Turley, M.J., Khanam, T., Aktas, T., Ramirez, F., Gendrel, A.V., Wright, P.R., Videm, P., Backofen, R., et al. (2014). MOF-associated complexes ensure stem cell identity and Xist repression. *eLife* 3, e02024.
- Chen, Z., Ye, X., Tang, N., Shen, S., Li, Z., Niu, X., Lu, S., and Xu, L. (2014). The histone acetyltransferase hMOF acetylates Nrf2 and regulates anti-drug responses in human non-small cell lung cancer. *Br. J. Pharmacol.* 171, 3196–3211.
- Conrad, T., and Akhtar, A. (2011). Dosage compensation in *Drosophila melanogaster*: epigenetic fine-tuning of chromosome-wide transcription. *Nat. Rev. Genet.* 13, 123–134.
- Di Giorgio, E., and Brancolini, C. (2016). Regulation of class IIa HDAC activities: it is not only matter of subcellular localization. *Epigenomics* 8, 251–269.
- Feller, C., Prestel, M., Hartmann, H., Straub, T., Söding, J., and Becker, P.B. (2012). The MOF-containing NSL complex associates globally with house-keeping genes, but activates only a defined subset. *Nucleic Acids Res.* 40, 1509–1522.
- Fernández-Silva, P., Acín-Pérez, R., Fernández-Vizcarra, E., Pérez-Martos, A., and Enriquez, J.A. (2007). In vivo and in organello analyses of mitochondrial translation. *Methods Cell Biol.* 80, 571–588.
- Füllgrabe, J., Lynch-Day, M.A., Heldring, N., Li, W., Struijk, R.B., Ma, Q., Hermanson, O., Rosenfeld, M.G., Klionsky, D.J., and Joseph, B. (2013). The histone H4 lysine 16 acetyltransferase hMOF regulates the outcome of autophagy. *Nature* 500, 468–471.
- Gilsbach, R., Preissl, S., Grüning, B.A., Schnick, T., Burger, L., Benes, V., Würch, A., Bönisch, U., Günther, S., Backofen, R., et al. (2014). Dynamic DNA methylation orchestrates cardiomyocyte development, maturation and disease. *Nat. Commun.* 5, 5288.
- Gu, W., Szauter, P., and Lucchesi, J.C. (1998). Targeting of MOF, a putative histone acetyl transferase, to the X chromosome of *Drosophila melanogaster*. *Dev. Genet.* 22, 56–64.
- Gupta, A., Sharma, G.G., Young, C.S., Agarwal, M., Smith, E.R., Paull, T.T., Lucchesi, J.C., Khanna, K.K., Ludwig, T., and Pandita, T.K. (2005). Involvement of human MOF in ATM function. *Mol. Cell. Biol.* 25, 5292–5305.
- Gupta, A., Guerin-Peyrou, T.G., Sharma, G.G., Park, C., Agarwal, M., Ganju, R.K., Pandita, S., Choi, K., Sukumar, S., Pandita, R.K., et al. (2008). The mammalian ortholog of *Drosophila* MOF that acetylates histone H4 lysine 16 is essential for embryogenesis and oncogenesis. *Mol. Cell. Biol.* 28, 397–409.
- Hilfiker, A., Hilfiker-Kleiner, D., Pannuti, A., and Lucchesi, J.C. (1997). mof, a putative acetyl transferase gene related to the Tip60 and MOZ human genes and to the SAS genes of yeast, is required for dosage compensation in *Drosophila*. *EMBO J.* 16, 2054–2060.
- Johnston, A.J., Hoogenraad, J., Dougan, D.A., Truscott, K.N., Yano, M., Mori, M., Hoogenraad, N.J., and Ryan, M.T. (2002). Insertion and assembly of human tom7 into the preprotein translocase complex of the outer mitochondrial membrane. *J. Biol. Chem.* 277, 42197–42204.
- Kadlec, J., Hallaceli, E., Lipp, M., Holz, H., Sanchez-Weatherby, J., Cusack, S., and Akhtar, A. (2011). Structural basis for MOF and MSL3 recruitment into the dosage compensation complex by MSL1. *Nat. Struct. Mol. Biol.* 18, 142–149.
- Kalashnikova, A.A., Porter-Goff, M.E., Muthurajan, U.M., Luger, K., and Hansen, J.C. (2013). The role of the nucleosome acidic patch in modulating higher order chromatin structure. *J. R. Soc. Interface* 10, 20121022.
- Kapoor-Vazirani, P., Gagey, J.D., Powell, D.R., and Vertino, P.M. (2008). Role of hMOF-dependent histone H4 lysine 16 acetylation in the maintenance of TMS1/ASC gene activity. *Cancer Res.* 68, 6810–6821.
- Kirches, E. (2011). LHON: Mitochondrial Mutations and More. *Curr. Genomics* 12, 44–54.
- Koolen, D.A., Kramer, J.M., Neveling, K., Nillesen, W.M., Moore-Barton, H.L., Elmslie, F.V., Toutain, A., Amiel, J., Malan, V., Tsai, A.C., et al. (2012). Mutations in the chromatin modifier gene KANSL1 cause the 17q21.31 microdeletion syndrome. *Nat. Genet.* 44, 639–641.
- Lam, K.C., Mühlplfordt, F., Vaquerizas, J.M., Raja, S.J., Holz, H., Luscombe, N.M., Manke, T., and Akhtar, A. (2012). The NSL complex regulates house-keeping genes in *Drosophila*. *PLoS Genet.* 8, e1002736.
- Leigh-Brown, S., Enriquez, J.A., and Odom, D.T. (2010). Nuclear transcription factors in mammalian mitochondria. *Genome Biol.* 11, 215.

- Li, X., Wu, L., Corsa, C.A., Kunkel, S., and Dou, Y. (2009). Two mammalian MOF complexes regulate transcription activation by distinct mechanisms. *Mol. Cell* **36**, 290–301.
- Love, M.I., Huber, W., and Anders, S. (2014). Moderated estimation of fold change and dispersion for RNA-seq data with DESeq2. *Genome Biol.* **15**, 550.
- Lucchesi, J.C., and Kuroda, M.I. (2015). Dosage compensation in *Drosophila*. *Cold Spring Harb. Perspect. Biol.* **7**, a019398.
- Lyons, G.E., Mühlebach, S., Moser, A., Masood, R., Paterson, B.M., Buckingham, M.E., and Perriard, J.C. (1991). Developmental regulation of creatine kinase gene expression by myogenic factors in embryonic mouse and chick skeletal muscle. *Development* **113**, 1017–1029.
- Martell, J.D., Deerinck, T.J., Sancak, Y., Poulos, T.L., Mootha, V.K., Sosinsky, G.E., Ellisman, M.H., and Ting, A.Y. (2012). Engineered ascorbate peroxidase as a genetically encoded reporter for electron microscopy. *Nat. Biotechnol.* **30**, 1143–1148.
- Mendjan, S., Taipale, M., Kind, J., Holz, H., Gebhardt, P., Scheider, M., Vermeulen, M., Buscaino, A., Duncan, K., Mueller, J., et al. (2006). Nuclear pore components are involved in the transcriptional regulation of dosage compensation in *Drosophila*. *Mol. Cell* **21**, 811–823.
- Mercer, T.R., Neph, S., Dinger, M.E., Crawford, J., Smith, M.A., Shearwood, A.M., Haugen, E., Bracken, C.P., Rackham, O., Stamatoyannopoulos, J.A., et al. (2011). The human mitochondrial transcriptome. *Cell* **146**, 645–658.
- Meunier, S., Shvedunova, M., Van Nguyen, N., Avila, L., Vernos, I., and Akhtar, A. (2015). An epigenetic regulator emerges as microtubule minus-end binding and stabilizing factor in mitosis. *Nat. Commun.* **6**, 7889.
- Mootha, V.K., Lindgren, C.M., Eriksson, K.F., Subramanian, A., Sihag, S., Lehhar, J., Puigserver, P., Carlsson, E., Ridderstråle, M., Laurila, E., et al. (2003). PGC-1 α -responsive genes involved in oxidative phosphorylation are coordinately downregulated in human diabetes. *Nat. Genet.* **34**, 267–273.
- Omura, T. (1998). Mitochondria-targeting sequence, a multi-role sorting sequence recognized at all steps of protein import into mitochondria. *J. Biochem.* **123**, 1010–1016.
- Perales-Clemente, E., Fernández-Vizarrá, E., Acín-Pérez, R., Movilla, N., Bayona-Bafaluy, M.P., Moreno-Loshuertos, R., Pérez-Martos, A., Fernández-Silva, P., and Enriquez, J.A. (2010). Five entry points of the mitochondrially encoded subunits in mammalian complex I assembly. *Mol. Cell. Biol.* **30**, 3038–3047.
- Pfister, S., Rea, S., Taipale, M., Mendrzyk, F., Straub, B., Ittrich, C., Thuerigen, O., Sinn, H.P., Akhtar, A., and Lichter, P. (2008). The histone acetyltransferase hMOF is frequently downregulated in primary breast carcinoma and medulloblastoma and constitutes a biomarker for clinical outcome in medulloblastoma. *Int. J. Cancer* **122**, 1207–1213.
- Plagg, B., Ehrlich, D., Kniewallner, K.M., Marksteiner, J., and Humpel, C. (2015). Increased Acetylation of Histone H4 at Lysine 12 (H4K12) in Monocytes of Transgenic Alzheimer's Mice and in Human Patients. *Curr. Alzheimer Res.* **12**, 752–760.
- Preissl, S., Schwaderer, M., Raulf, A., Hesse, M., Gruning, B.A., Kobele, C., Backofen, R., Fleischmann, B.K., Hein, L., and Gilsbach, R. (2015). Deciphering the epigenetic code of cardiac myocyte transcription. *Circ. Res.* **117**, 413–423.
- Qiao, W., Zhang, W., Gai, Y., Zhao, L., and Fan, J. (2014). The histone acetyltransferase MOF overexpression blunts cardiac hypertrophy by targeting ROS in mice. *Biochem. Biophys. Res. Commun.* **448**, 379–384.
- Raja, S.J., Charapitsa, I., Conrad, T., Vaquerizas, J.M., Gebhardt, P., Holz, H., Kadlec, J., Fraterman, S., Luscombe, N.M., and Akhtar, A. (2010). The nonspecific lethal complex is a transcriptional regulator in *Drosophila*. *Mol. Cell* **38**, 827–841.
- Ravens, S., Fournier, M., Ye, T., Stierle, M., Dembele, D., Chavant, V., and Tora, L. (2014). Mof-associated complexes have overlapping and unique roles in regulating pluripotency in embryonic stem cells and during differentiation. *eLife* **3**, e02104.
- Rhee, H.W., Zou, P., Udeshi, N.D., Martell, J.D., Mootha, V.K., Carr, S.A., and Ting, A.Y. (2013). Proteomic mapping of mitochondria in living cells via spatially restricted enzymatic tagging. *Science* **339**, 1328–1331.
- Robinson, B.H., Petrova-Benedict, R., Buncic, J.R., and Wallace, D.C. (1992). Nonviability of cells with oxidative defects in galactose medium: a screening test for affected patient fibroblasts. *Biochem. Med. Metab. Biol.* **48**, 122–126.
- Rugarli, E.I., and Langer, T. (2012). Mitochondrial quality control: a matter of life and death for neurons. *EMBO J.* **31**, 1336–1349.
- Shogren-Knaak, M., Ishii, H., Sun, J.M., Pazin, M.J., Davie, J.R., and Peterson, C.L. (2006). Histone H4-K16 acetylation controls chromatin structure and protein interactions. *Science* **311**, 844–847.
- Shutt, T.E., and Shadel, G.S. (2010). A compendium of human mitochondrial gene expression machinery with links to disease. *Environ. Mol. Mutagen.* **51**, 360–379.
- Soonpaa, M.H., Kim, K.K., Pajak, L., Franklin, M., and Field, L.J. (1996). Cardiomyocyte DNA synthesis and binucleation during murine development. *Am. J. Physiol.* **271**, H2183–H2189.
- Subramanian, A., Tamayo, P., Mootha, V.K., Mukherjee, S., Ebert, B.L., Gillette, M.A., Paulovich, A., Pomeroy, S.L., Golub, T.R., Lander, E.S., et al. (2005). Gene set enrichment analysis: a knowledge-based approach for interpreting genome-wide expression profiles. *Proc. Natl. Acad. Sci. USA* **102**, 15545–15550.
- Sykes, S.M., Mellert, H.S., Holbert, M.A., Li, K., Marmorstein, R., Lane, W.S., and McMahon, S.B. (2006). Acetylation of the p53 DNA-binding domain regulates apoptosis induction. *Mol. Cell* **24**, 841–851.
- Szczepanek, K., Lesnefsky, E.J., and Larner, A.C. (2012). Multi-tasking: nuclear transcription factors with novel roles in the mitochondria. *Trends Cell Biol.* **22**, 429–437.
- Taipale, M., Rea, S., Richter, K., Vilar, A., Lichter, P., Imhof, A., and Akhtar, A. (2005). hMOF histone acetyltransferase is required for histone H4 lysine 16 acetylation in mammalian cells. *Mol. Cell. Biol.* **25**, 6798–6810.
- Thomas, T., Dixon, M.P., Kueh, A.J., and Voss, A.K. (2008). Mof (MYST1 or KAT8) is essential for progression of embryonic development past the blastocyst stage and required for normal chromatin architecture. *Mol. Cell. Biol.* **28**, 5093–5105.
- Tighe, A., Staples, O., and Taylor, S. (2008). Mps1 kinase activity restrains anaphase during an unperturbed mitosis and targets Mad2 to kinetochores. *J. Cell Biol.* **181**, 893–901.
- Trask, R.V., and Billadello, J.J. (1990). Tissue-specific distribution and developmental regulation of M and B creatine kinase mRNAs. *Biochim. Biophys. Acta* **1049**, 182–188.
- Vögtle, F.N., Wortelkamp, S., Zahedi, R.P., Becker, D., Leidhold, C., Gevaert, K., Kellermann, J., Voos, W., Sickmann, A., Pfanner, N., and Meisinger, C. (2009). Global analysis of the mitochondrial N-proteome identifies a processing peptidase critical for protein stability. *Cell* **139**, 428–439.
- Wang, Z., Ying, Z., Bosy-Westphal, A., Zhang, J., Schautz, B., Later, W., Heymsfield, S.B., and Müller, M.J. (2010). Specific metabolic rates of major organs and tissues across adulthood: evaluation by mechanistic model of resting energy expenditure. *Am. J. Clin. Nutr.* **92**, 1369–1377.
- Wenz, L.S., Ellenrieder, L., Qiu, J., Bohnert, M., Zufall, N., van der Laan, M., Pfanner, N., Wiedemann, N., and Becker, T. (2015). Sam37 is crucial for formation of the mitochondrial TOM-SAM supercomplex, thereby promoting beta-barrel biogenesis. *J. Cell Biol.* **210**, 1047–1054.

STAR★METHODS

KEY RESOURCES TABLE

REAGENT or RESOURCE	SOURCE	IDENTIFIER
Antibodies		
COX IV, Rb mAb (Clone 3E11)	Cell signaling	Cat#4850; RRID: AB_2085424
CYT-C, Rb pAb	This paper, raised in laboratory of N.Pfanner/ T.Becker	N/A
dsDNA, Ms mAb (35I9 DNA)	Abcam	Cat#ab27156; RRID: AB_470907
GAPDH, Rb pAb	Bethyl	Cat#A300-641A; RRID: AB_513619
GRP75, Rb pAb	This paper, raised in laboratory of N.Pfanner/ T.Becker	N/A
H3, Rb pAb	Abcam	Cat#ab1791; RRID: AB_302613
H4K12ac, Rb pAb	Millipore	Cat#07-595; RRID: AB_310740
H4K16ac, Rb pAb	Millipore	Cat#07329; RRID: AB_310525
H4K5ac, Rb pAb	Millipore	Cat#07327; RRID: AB_11210470
H4K8ac, Rb pAb	Abcam	Cat#ab15823; RRID: AB_880455
HP1, Rb pAb	Kind gift from Dr. Thomas Jenuwein	N/A
HSP60, Rb pAb	This paper, raised in laboratory of N.Pfanner/ T.Becker	N/A
KANSL1, Rt pAb	(Mendjan et al., 2006)	N/A
KANSL1, Rb pAb	Abnova	Cat#PAB20355; RRID: AB_10984400
KANSL3, Rb pAb	Sigma Aldrich	Cat#HPA035018; RRID: AB_10601763
KANSL3, Rb pAb	(Mendjan et al., 2006)	N/A
MCRS1, Rb pAb	Proteintech	Cat#11362-1-AP; RRID: AB_2143116
MIA40, Rb pAb	This paper, raised in laboratory of N.Pfanner/ T.Becker	N/A
MOF, Rt pAb	(Taipale et al., 2005; Pfister et al., 2008)	N/A
MOF, Rb pAb	Bethyl	Cat#A300-992A; RRID: AB_805802
MTPAP, Ms mAb (Clone 1D3)	Acris	Cat#GTX70156; RRID: AB_11164518
NDUFA9, Rb pAb	This paper, raised in laboratory of N.Pfanner/ T.Becker	N/A
Pan acetyl lysine, Rb pAb	Cell signaling	Cat#9441; RRID: AB_331806
PCM1, Rb pAb	Sigma Aldrich	Cat#HPA023370; RRID: AB_1855072
POLG, Rb pAb	Acris	Cat#GTX100398; RRID: AB_1240719
POLRMT, Rb pAb	Abcam	Cat#ab93102; RRID: AB_10563343
POLRMT, Rb pAb (N2N3)	Acris	Cat#GTX105137; RRID: AB_2037731
SSBP1, Rb pAb	Proteintech	Cat#12212-1- AP; RRID: AB_2195320
TFAM, Rb pAb	Millipore	Cat#ABE483
TFB2M, Rb pAb (C3)	Acris	Cat#GTX107714; RRID: AB_1241385
TOM20, Rb pAb (FL-145)	Santa Cruz	Cat#sc-11415; RRID: AB_2207533
α Tubulin, Ms mAb	Abcam	Cat#44928; RRID: AB_2241150
α Tubulin, Rb mAb (clone EP1332Y)	Millipore	Cat#04-1117; RRID: AB_1977540
α Tubulin, Ms mAb (YL1/2)	Santa Cruz	Cat#sc-53029; RRID: AB_793541
Chemicals, Peptides, and Recombinant Proteins		
Galactose	Sigma Aldrich	G5388
Oligomycin	Sigma Aldrich	75351
FCCP	Sigma Aldrich	C2920
Rotenone	Sigma Aldrich	R8875
Antimycin A	Sigma Aldrich	A0149

(Continued on next page)

Continued

REAGENT or RESOURCE	SOURCE	IDENTIFIER
Dihydroethidium (DHE)	Thermo Fisher	D11347
JC-1 Dye	Thermo Fisher	T3168
MitoTracker red CMXRos	Life technologies	M751
Critical Commercial Assays		
Seahorse XF Mito Fuel Flex Test Kit	Seahorse Biosciences (Agilent technologies)	103260-100
Click-iT Nascent RNA Capture Kit	Thermo Fisher C10365	C10365
TruSeq stranded mRNA sample preparation kit	Illumina	RS-122- 2101
Nugen Ovation RNA-seq System V2 kit	Nugen	7102-08
NEBNext Ultra DNA Library Prep Kit	New England Biolabs	E7370L
RNeasy Micro Kit	QIAGEN	74004
Deposited Data		
RNA-seq data	This paper	GEO: GSE77784
Experimental Models: Cell Lines		
HeLa alpha Kyoto cells	BIOSS excellence cluster	N/A
HeLa Flp-In T-Rex host cells	Stephen Taylor, University of Manchester (Tighe et al., 2008)	N/A
wtMOF-sfGFP cell line	This paper	N/A
wtMOF-sfGFP cell line	This paper	N/A
MTS-wtMOF-sfGFP cell line	This paper	N/A
MTS-MOF(Δ NLS1)-sfGFP cell line	This paper	N/A
MTS-MOF(Δ NLS1, E350Q)-sfGFP cell line	This paper	N/A
sfGFP cell line	This paper	N/A
Experimental Models: Organisms/Strains		
Mouse: <i>Mo^{f1/f1}</i>	(Thomas et al., 2008)	N/A
Mouse: FVB-Tg (Ckm-cre) 5Khn/J	The Jackson Laboratory	JAX:006405
Recombinant DNA		
wtMOF-sfGFP	This paper	N/A
MTS-wtMOF-sfGFP	This paper	N/A
MTS-MOF(Δ NLS1)-sfGFP	This paper	N/A
MTS-MOF(Δ NLS1, E350Q)-sfGFP	This paper	N/A
sfGFP	This paper	N/A
Plasmid backbone: pcDNA5/FRT/TO	Life technologies	V652020
Sequence-Based Reagents		
siSCRAM (5'-CGAGGAAGGAUUGAUAGA-3')	This paper	N/A
siMOF-1 (5'-GGAAUUCUAUGUACACUAC-3')	This paper	N/A
siMOF-2 (5'-GUGAUCCAGUCUCGAGUGA-3')	(Taipale et al., 2005)	N/A
siKANSL1-1 (5'-CGGCAACGCCAACAUCUU-3')	(Meunier et al., 2015)	N/A
siKANSL1-2 (5'GAAGCGGAGGCUUGUUCGA-3')	(Meunier et al., 2015)	N/A
siKANSL3-1 (5'-GGCACGCAGCGUGAUGAAU-3')	(Meunier et al., 2015)	N/A
siKANSL3-2 (5'-GGCACGCAGCGUGAUGAAU-3')	(Meunier et al., 2015)	N/A
Primers are listed in Table S1	This paper	N/A

(Continued on next page)

Continued		
REAGENT or RESOURCE	SOURCE	IDENTIFIER
Software and Algorithms		
DESeq2 (v1.8.2)	(Love et al., 2014)	https://bioc.ism.ac.jp/packages/3.1/bioc/html/DESeq2.html
GSEA software (v.2.2.1)	(Subramanian et al., 2005; Mootha et al., 2003)	http://software.broadinstitute.org/gsea/index.jsp
Ingenuity Pathway Analysis (IPA)	QIAGEN	http://www.ingenuity.com/
Prism 6	GraphPad Software	http://www.graphpad.com/scientific-software/prism/

CONTACT FOR REAGENT AND RESOURCE SHARING

Further information and requests for reagents may be directed to, and will be fulfilled by the corresponding author Asifa Akhtar (akhtar@ie-freiburg.mpg.de).

EXPERIMENTAL MODEL AND SUBJECT DETAILS

Mouse Strains

Cardiomyocyte specific Mof-knockout mice were generated by crossing *Mof* allele (*Mof*^{fl^{ox}}) (Thomas et al., 2008) with mice carrying the *Ckm-cre* [JAX #006405: FVB-Tg (*Ckm-cre*) 5Khn/J] transgene. All animal procedures were approved by the responsible animal care committees (Regierungspräsidium Freiburg, Karlsruhe/Germany), and they conformed to the Guide for the Care and Use of Laboratory Animals published by the NIH (publication No. 85-23, revised 1996). The age and sex of animals used in various studies is mentioned in the relevant method details sections.

Plasmids and Cell Lines

HeLa alpha Kyoto cells were obtained from cell line depository of BIOSSE excellence cluster (Freiburg, Germany).

The wtMOF-sfGFP; MTS-wtMOF-sfGFP; MTS-MOF(Δ NLS1)-sfGFP, MTS-MOF(Δ NLS1,E350Q)-sfGFP; sfGFP and MTS-sfGFP sequences were cloned into pcDNA5/FRT/TO vector (expresses Flp-3In). These plasmids were used to generate HeLa cell lines using the Flp-In T-Rex technology (Life Technologies). They were co-transfected (with pOG44 (expresses Flp recombinase) into host HeLa Flp-In T-Rex cells (a kind gift of Stephen Taylor, University of Manchester (Tighe et al., 2008)) to generate stable inducible cell lines. The lines were maintained in 4 μ g/mL blasticidin and 200 μ g/mL hygromycin B; and induced with 0.1 μ g/mL doxycycline (DOX) 16-20 hr before the experiment. The drugs were purchased from Sigma Aldrich. Superfolder GFP (sfGFP) sequence was obtained from SnapGene (<http://www.snapgene.com/>).

NOTE: All MOF constructs had synonymous mutations, to make them insensitive to siMOF RNAs used in this paper; MTS represents COX4 mitochondrial targeting signal: *MLATRVFSLVGKRAISTSVCVRAH*; NLS1 denotes nuclear localization signal1 of human MOF and Δ NLS1 is its mutated version (See: *Prediction of nuclear localization signal*).

METHOD DETAILS

Cell Culture and Maintenance

HeLa alpha Kyoto and DOX inducible cell lines were cultured in the following media conditions:

Glucose media

High glucose DMEM (Life technologies #DMEM 10566-016), 100 U/ml penicillin, 100 μ g/ml streptomycin and 10% fetal bovine serum (FBS).

Galactose media

Glucose free DMEM (Life technologies #11966025) base media supplemented with 1 M galactose (Sigma #G5388), 4 mM glutamine, 5 mM HEPES, 1 mM sodium pyruvate, 100 U/ml penicillin, 100 μ g/ml streptomycin and 10% FBS. Unless otherwise mentioned, the additives were from Life Technologies.

HeLa Flp-In T-Rex host cells were verified by Tighe et al., 2008. They were maintained with additional 4 μ g/mL blasticidin and zeocin 50 μ g/mL in glucose/galactose media. HeLa Flp-In T-Rex cell lines were maintained in 4 μ g/mL blasticidin and 200 μ g/mL hygromycin B. To minimize leaky expression of transgene, cell lines were cultured in tetracycline-free FBS (PAN Biotech #P30-3602).

Immunocytochemistry and confocal microscopy

Cells were prepared for immunocytochemistry using standard methods. Briefly, the cells were fixed with pre-warmed 4% formaldehyde (Thermo #28906) for 9 min at 37°C followed by 2-3 washes in 1x PBS (Life #10010023). They were then permeabilized with 0.2%

Triton (Sigma #T8787)/ PBS solution for 5 min at 22–25°C, before blocking for 1 hr with 5% BSA (Sigma #BSAVHS-RO) in 0.05% Triton/ PBS solution. All primary antibodies were incubated overnight for staining at 4°C in the same blocking solution. Next day, they were washed, stained with appropriate secondary antibodies for 1hr and washed again before imaging. Washes were of 5 min each in 0.05% Triton/PBS solution, thrice after primary and secondary antibody incubations. For cells stained with MitoTracker red CMXRos dye (Life technologies #M7512), mitochondria were labeled with 1 μ M of the dye for 1 hr at 37°C and 5% CO₂. Prior to fixation, they were washed twice with 1x PBS. Primary antibodies against Tubulin (Millipore #41117, abcam #44928 & Santa cruz #53029), DNA (abcam #ab27156) and TOM20 (Santa cruz #11415) were used. Antibodies against MOF (Taipale et al., 2005; Pfister et al., 2008), KANSL1 and KANSL3 (Mendjan et al., 2006) have been described previously. DAPI and the secondary antibodies (Alexa Fluor 647 and 488 conjugates) were from Molecular Probes. Confocal images were acquired with Zeiss Observer Z1, an inverted spinning disk microscope equipped with CSU-X1 scan head (Yokogawa) and an EM-CCD camera, using standard filter sets. Images were analyzed using CellProfiler software (<http://cellprofiler.org>).

Note: We could obtain specific (knockdown sensitive) immunofluorescence signals for MOF, KANSL1 and KANSL3 only with antibodies mentioned in this section. Other commercially available antibodies (used in rest of the paper) were incompatible with our staining protocols.

Multi-color 3D high-resolution structured illumination microscopy (HR-SIM)

Samples were prepared in the same manner as described before. Images were acquired in Elyra PS1 microscope, which combines structured illumination module and LSM780 confocal scanning unit (Carl Zeiss), with a Plan-apochromat 100x oil 1.46 N.A. objective, and an Andor iXon DU 885 EM-CCD camera. Image stacks were acquired sequentially: first, HR-SIM images in far-red and green channels (642 and 488 nm excitation, respectively, and standard filter cubes), then confocal images in blue channel to visualize DAPI staining (excitation at 405 nm, emission 415–480 nm); voxel size and field of view of confocal images was set to exactly match those of HR-SIM images (50nm \times 50nm \times 100nm). Raw HR-SIM data were processed with Zen black 2012 software (Carl Zeiss) with automatically selected processing parameters; both super-resolved SIM and wide-field images were extracted from raw HR-SIM data. All color channels were aligned using reference images of multi-color fluorescence beads, which were acquired on the same day as respective experimental images.

Prediction of mitochondrial targeting sequences

We used MitoFates (<http://mitf.cbrc.jp/MitoFates/cgi-bin/top.cgi>) software to identify amphipathic alpha helices and TOM20 binding sites on proteins. Mitochondrial targeting sequence (MTS) for KANSL2 was determined using MitoProt II (<https://ihg.gsf.de/ihg/mitoprot.html>). MitoProt II software searches for sequence features associated with mitochondrial pre-sequences, as well as possibility of a cleavage site to make its predictions. As, Glu or Asp is often found within set distances from these sites, the software's search window is restricted to the amino acid preceding them. For KANSL3, the MTS was not determined with full-length protein. Based on the hypothesis that it might contain buried and/or uncleaved MTS (thus undermining the Glu or Asp based search criteria), we tweaked our search parameters and presented the software with sequentially cleaved versions of the protein. Thorough analysis of the first 500 amino acids of the protein, by recalculating the probabilities after removing one amino acid at a time, we revealed the cryptic MTS of human KANSL3.

MTS often possess a distinctive arrangement of hydrophobic and hydrophilic amino acid residues on opposite surfaces of a α -helix, typically located at the N terminus. We identified such amphipathic helices in all four NSL members analyzed. TOM20 binding sites were also predicted for MOF, KANSL2 and KANSL3 (Figure 1E). However, characteristic properties of a clear MTS were only identified for KANSL2 and KANSL3 (Figure 1E).

Prediction of nuclear localization signal (NLS)

Importin α -dependent nuclear localization signal (NLS) of hMOF (458 amino acids) was predicted using cNLS mapper software (http://nls-mapper.iab.keio.ac.jp/cgi-bin/NLS_Mapper_form.cgi). The entire length of the protein was included in the search and only predictions above the cutoff score of 6.0 were considered. Two NLS sequences were predicted- (1) position 140-RNQRKRDHDEI, score 10.5 and (2) A bipartite signal starting at position 177- KYVDKIHIIGNYEIDAWYFSPFPEDYGKQPKLW, score 6.7. They were denoted as NLS1 and NLS2 respectively in the manuscript (Figure 1H, bottom). Based on the prediction scores, we concluded NLS1 to be stronger of the two. Mutant form of NLS1 (Δ NLS1), used in different experiments has following sequence: ANQAAHDEI. Of note, NLS2 coincides with MOF's HAT domain, where mutations would lead to loss of function or instability of the protein (Kadlec et al., 2011).

Western blotting

Western blots were performed on different extracts as mentioned in the figures. Except kit based extracts, all other cellular lysates were prepared in same buffer (20mM HEPES pH7.4, 150mM NaCl, 1mM EDTA, 0.1% NP40 and 10% glycerol).

MOPS-based denaturing PAGE were used in western blots.

Primary antibodies used

MOF (Bethyl #A300-992A), KANSL1 (Abnova #PAB20355), KANSL3 (Sigma #HPA035018), MCRS1 (Proteintech #11362-1-AP), GAPDH (Bethyl #A300-641A), COX4 (Cell signaling #4850), TOM20 (Santa cruz #sc-11415), H3 (abcam #ab1971), H4K5ac (Millipore

#07327), H4K8ac (Active motif #39243), H4K12ac (Millipore #07595), H4K16ac (Millipore #07329), Pan acetyl lysine (Cell signaling #9441), TFAM (Millipore #ABE483), POLRMT (A) (abcam # ab93102), POLRMT (B) (Acris antibodies # GTX105137), TFB2M (Acris antibodies # GTX107714), MTPAP (Acris antibodies # GTX70156), POLG (Acris antibodies # GTX100398), SSBP (Proteintech #12212-1-AP). HP1 was a kind gift from T.Jenuwein; CYT-C, HSP60, NDUFA9, GRP75, MIA40 were raised in rabbits and the immunosignals were verified by western blotting using isolated mitochondria.

Protein import into yeast mitochondria

For in vitro import assays the yeast strains YPH499 and *tom20Δ* (Becker et al., 2011) were grown in YPG medium (1% (w/v) yeast extract, 2% (w/v) peptone, 3% (v/v) glycerol) and mitochondria were isolated by differential centrifugation (Wenz et al., 2015). The precursor proteins were labeled with [³⁵S] methionine by in vitro translation using cell free translation extract based on rabbit reticulocyte lysate (TNT, Promega). The radiolabeled precursor was incubated with isolated yeast mitochondria at 30°C in the presence of import buffer (0%–3% (w/v) BSA, 250 mM sucrose, 80 mM KCl, 5 mM MgCl₂, 5 mM methionine, 10 mM KH₂PO₄, 10 mM MOPS-KOH pH 7.2) containing 4 mM ATP, 2 mM NADH, 5 mM creatine phosphate and 100 μg/ml creatine kinase (Becker et al., 2011; Wenz et al., 2015). The import reaction was stopped by dissipation of the membrane potential with 8 μM antimycin A, 1 μM valinomycin and 20 μM oligomycin. Subsequently, non-imported precursor proteins were removed by incubation with proteinase K (final concentration of 20–50 μg/ml). The protease was inactivated by addition of PMSF to a final concentration of 1 mM. Mitochondria were re-isolated, washed with SEM-buffer and lysed under denaturing conditions. The radiolabeled proteins were detected by SDS-PAGE and autoradiography.

Blue native electrophoresis

For blue native electrophoresis, mitochondria were solubilized in 1% (w/v) digitonin in lysis buffer (20 mM Tris/HCl pH 7.4, 50 mM NaCl, 0.1 mM EDTA, 10% (v/v) glycerol) for 15 min on ice. Insoluble material was removed by centrifugation and subjected to blue native electrophoresis.

Cellular fractionation and knockdowns

Cellular fractionation to prepare cytosolic, mitochondrial, and nuclear extracts was performed using a kit (abcam #ab110170), according to manufacturer's instructions. siRNA mediated knockdowns were performed following standard protocols on 40% confluent HeLa cells (glucose or galactose adapted for minimum 2 weeks), using XtremeGENE siRNA transfection reagent (Roche). For MOF, KANSL1 and KANSL3 knockdowns, two siRNAs were mixed in equal proportions before experiment. Cells were harvested/ imaged after 3.5 days of knockdown.

Functional mitochondria isolation and purification

Mitochondrial isolation from cultured cells was based on a protocol modified from (Johnston et al., 2002) and all experiments were performed on maximally 80%–90% confluent dishes. Briefly, cells were first harvested by scraping in PBS on ice. Cell pellets were then suspended in 5x pellet-volume chilled mitochondria isolation buffer (MIB- 20 mM HEPES-KOH pH 7.4, 220 mM mannitol, 70 mM sucrose, 1 mM EDTA and 2 mg/ml BSA), supplemented with protease inhibitor mix (Roche) and dounced 20–30 times in type-B glass homogenizer. Nuclei and unbroken cells were pelleted at 800 g/ 10 min/ 4°C. Mitochondria was precipitated from the supernatant by centrifugation at 10,000 g/ 20 min/ 4°C. Crude mitochondrial pellet was washed twice with chilled mitochondria wash buffer (MWB- 20 mM HEPES-KOH pH 7.4, 220 mM mannitol, 70 mM sucrose and 1mM EDTA), before protein estimation and usage in downstream protocols. For localization verification studies, crude mitochondria were further purified using discontinuous (15%–50%) percoll (GE healthcare #17089101) gradient. Pure mitochondria were obtained from 22%–50% gradient interface, washed twice in MIB to remove percoll and used immediately in assays or stored at –80°C. Unless otherwise stated, all chemicals were purchased from Sigma.

In organello translation in isolated human mitochondria

The procedure of in organello translation in human mitochondria was modified from (Fernández-Silva et al., 2007). Isolated mitochondria were incubated in reaction buffer (25 mM sucrose, 75 mM sorbitol, 100 mM KCl, 1 mM MgCl₂, 0.05 mM EDTA, 10 mM Tris/HCl pH 7.4, 10 mM K₂HPO₄, 10 mM glutamate, 2.5 mM malate, 1 mM ADP, 1mg/ml BSA) containing 100 μg/ml cycloheximide and an amino acid mixture lacking methionine (final conc. 20 μM) for 5 min at 37°C. To start the reaction ³⁵S-labeled methionine was added and the samples were incubated for different time periods at 37°C. The in organello translation was stopped by addition of cold methionine (10 mM final conc.) and incubation for 5 min at 37°C. Subsequently, mitochondria were re-isolated and washed twice with 320 mM sucrose, 1mM EDTA and 10 mM Tris/HCl pH 7.4. The mitochondrial pellet was lysed under denaturing conditions and proteins were detected by Tris/Tricine-SDS-PAGE and autoradiography.

Proteinase K protection assay

Freshly isolated mitochondria were the starting point of this assay. First, 100 μg of mitochondria were suspended in 100 μl of each of the three following buffers: (1) Iso-osmotic (10 mM MOPS-KOH pH 7.2, 250 mM sucrose, 1 mM EDTA), (2) Hypo-osmotic (10 mM MOPS-KOH pH 7.2, 1 mM EDTA) and (3) Membrane perforated (10 mM Tris-HCl, 1mM EDTA, 1% Triton X-100). 20 μg/ml proteinase

K was added to each of them and incubated for 15 mins on ice. Reactions were stopped with 20 mM PMSF; samples (1) and (2) were spun down at 10,000 g/ 15 min/ 4°C and pellets were collected. All three reaction sets were then solubilized in final 1x Laemmli loading buffer and made up to equal volumes before loading onto 4%–12% Bis-Tris gradient gels (Life technologies). Solutions were made using chemicals purchased from Sigma.

Nucleic acid extraction and quantitative RT PCR

All steps were performed using appropriate kit protocols. *For cultured cells*: RNA was extracted using Trizol reagent (Life technologies #10296010) and treated with Turbo DNase (Life technologies #AM2238) before performing reverse transcription using SuperScript III enzyme (Invitrogen #18080093). In experiments with parallel analysis of DNA, all prep DNA/RNA kit (QIAGEN #80204) was used and the RNA was processed as before. DNA was treated with RNase (Thermo # EN0531) before analysis. Quantitative real-time PCR was performed with FastStart SYBR mix (Roche #04913850001). *For mouse tissues*: RNA was isolated using the RNeasy fibrous tissue kit (QIAGEN #74704); reverse transcription and qPCR were performed using appropriate QIAGEN reagents.

RNA decay and turnover experiment

The experiment is divided into four major stages as follows:

Stage 1, Knockdowns & RNA labelling

MOF and scramble (control) knockdowns were performed with specific siRNAs in the same manner as mentioned before. After 72 hr of knockdown cells (RNA) were labeled with 0.2 mM 5-Ethynyl uridine (EU) in the following manner:

RNA synthesis study- Samples were labeled with EU supplemented growth media for either 4 hr (T1) or 5 hr (T2), without replacing the media. For analysis, the relative RNA synthesis was calculated for 5 hr over 4 hr pulse duration.

RNA turnover study- Samples were labeled with EU supplemented growth media for 3 hr (pulse, P). Next, they were washed with normal culture growth media and allowed to grow for 24 hr (chase, C) in the label-free growth media.

RNA samples: T1, T2, P and C were harvested for each sample set by Trizol following manufacturer's instructions. From here on, the Click-iT® Nascent RNA Capture Kit (Thermo #C10365) protocol was followed with slight modifications to the manufacturer's protocol.

Stage 2, RNA tagging

500 ng RNA was used in a Cu (I) mediated click reaction. At this stage, only EU labeled RNA population (synthesized during the labeling periods of stage1) was tagged with biotin. The click reaction was performed in 10 mM Tris-Cl buffer (pH 8.4), instead of the kit-supplied buffer, for 2 hr at 25°C. Rest of additives were added according to the manufacturer's instructions.

Stage 3, Tagged RNA capture

100 ng biotinylated RNA from previous stage was pulled down using MyOne T1 Streptavidin beads, following the manufacturer's protocols.

Stage 4, cDNA synthesis

The captured RNA on the streptavidin beads was converted to cDNA with random hexamers and RT mix mentioned before. qPCR analysis was performed in the same manner as mentioned before.

Determination of mitochondrial membrane potential by JC-1 staining

JC-1 is a potentiometric dye, which at low concentrations exists as a monomer emitting green fluorescence (525 nm). At higher concentrations (above $\Psi_m \sim 80$ -100 mV), it forms reversible aggregates (J-aggregates) and emits red fluorescence (590 nm). To determine mitochondrial membrane potential cells were stained live in normal growth media with 10 $\mu\text{g/ml}$ of JC-1 for 10 min at 37°C and imaged according to manufacturer's instruction. For analysis, at least 100 cells were selected from each field of view.

Bioenergetic profiling of cells

Cellular respiration was studied using the Seahorse XFe 96 analyzer (Seahorse Biosciences, Agilent technologies) using manufacturer's recommended protocols. Briefly, 20,000 (galactose adapted) or 40,000 (glucose adapted) cells were seeded in assay microplates, the night before. Next day, the cells were incubated in 160 μl of assay media, at 37°C in a CO₂ free incubator for 1 hr, just before the assay run. The plates were assayed on the XFe 96 analyzer, to calculate oxygen consumption rate (OCR) over time after sequential addition of different respiratory poisons. All respiratory drugs were purchased from Sigma; their final concentrations in the assay were: oligomycin (1 μM), FCCP (0.5 μM), rotenone (1 μM) and antimycin A (1 μM). After the run, assay media was removed and cell were lysed for analysis. The data were normalized with protein estimation (Bradford assay, Bio-Rad). We also validated the same with DNA normalization and found no difference.

Fuel dependency and flexibility assay

The assay was performed using Seahorse XF Mito Fuel Flex Test Kit (Seahorse Biosciences #103260-100) following the manufacturer's protocols. The assay media was matched to the cellular growth condition. Final concentrations of various inhibitors used is as follows: Mitochondrial pyruvate carrier inhibitor, UK5099- 2 μM ; Glutaminease I inhibitor, BPTES- 3 μM ; carnitine palmitoyl-transferase 1A inhibitor, Etomoxir- 4 μM .

Assay media composition

XF Base media (Seahorse Biosciences # 102353-100) was used to prepare the assay media. To this, 1 mM Sodium Pyruvate, 4 mM GlutaMax was added along with a following sugar concentration (depending on the cell growth conditions):

- a) Galactose adapted cells- 10 mM galactose
- b) Glucose adapted cells- 5.5 mM glucose

All additives were purchased from Sigma.

mtDNA immunoprecipitation (mtDIP)

We developed mtDIP protocol with modifications to previously described ChIP technique (Chelmicki et al., 2014).

*Described before in mitochondria isolation protocol.

Fixation

Mitochondrial pellets* were crosslinked in 1% formaldehyde (Thermo) for 9mins at RT, with gentle rotation. The reaction was quenched with (0.125 M) glycine for 4 min and mitochondria were spun down at 10,000 g/ 20 min/ 4°C. The pellets were washed twice with chilled MWB* before estimating their approximate dry weight.

Extract preparation

Mitochondrial pellets were suspended in 20x (w/v) RIPA lysis buffer (1x PBS, 1% NP-40, 0.5% sodium deoxycholate and 0.1% SDS) with protease inhibitors (Roche). mtDNA was sheared for 20 cycles, high settings in Bioruptor (Diagenode). Alternatively, they were sheared in Covaris (E220). 20-25 mg of mitochondria (dry weight) was sheared in 1 ml volume with following settings: burst- 200 / duty cycle- 20% / power- 150 W / time- 300 s. The appropriate cycle number (minimum number) was decided just after we observed the disappearance of 16Kb mtDNA into a smear. We estimated the DNA amount in every 1 mg (dry weight) mitochondrial extract and used 1 µg mtDNA for IP.

Immunoprecipitation

The extract was pre-cleared in 20 µl of beads (pre-equilibrated with RIPA) for 1 hr at 4°C and beads were spun down. IP was performed on the supernatant, with 4 µg of primary antibody at 4°C, overnight. Next day, 20 µl of RIPA-equilibrated beads were added to the extracts and incubated for 3 hr at 4°C.

Washing and Elution

The beads from last step were washed in following scheme- 4x, 15 min each, with RIPA; 2x, 1 min each, with LiCl buffer (250 mM LiCl, 10 mM Tris-Cl pH 8.0, 1 mM EDTA, 0.5% NP-40 and 0.5% DOC); 2x, 1 min each, with TE buffer (1mM Tris-Cl pH 8.0 and 1 mM EDTA). The beads were then subjected to RNase and proteinase K digestion in NaHCO₃ / SDS elution buffer and decrosslinked for 6h or overnight at 55°C. Finally, DNA was purified from the elution buffer, using kit-based protocol (PCR purification kit, QIAGEN). qPCR analysis was performed using FastStart SYBR mix (Roche) with input DNA used for normalization.

Antibodies used

MOF (Bethyl #A300-992A), KANSL3 (Sigma #HPA035018), TFAM (Merck Millipore #ABE483), POLRMT (A) (abcam # ab93102), POLRMT (B) (Acris antibodies # GTX105137), TFB2M (Acris antibodies # GTX107714), MTPAP (Acris antibodies # GTX70156), POLG (Acris antibodies # GTX100398), SSBP (Proteintech #12212-1-AP).

Ethidium bromide (EtBr) treatment

Cells were treated with 250 ng/ ml ethidium bromide diluted in the cell culture media for 6 hr. Following the treatment, samples were processed for western blotting or mtDIP as per protocols mentioned before.

Data visualization of mouse ChIP-seq profiles

ChIP-seq analysis was performed as described in Chelmicki et al. (2014). Circos software (<http://circos.ca/software/>) was used to visualize the binding of the ChIP signals on mouse mtDNA (mm10).

Rescue experiments

To address the question whether mitochondrial pool of the protein can rescue, we generated specific inner membrane/ matrix tethered constructs. Since, the specific localization was a major crux of the experiment, we used the well-established COX4 mitochondrial targeting sequence, MTS: (MLATRVFSLVGKRAISTSVCVRAH) as a synthetic tether. This has been very well established as a mitochondrial matrix tether sequence. Previous publications have verified its targeting properties by electron microscopic visualization (Martell et al., 2012) as well as mass spectrometry analysis (Rhee et al., 2013).

Experimental Optimization

MOF and scramble (control) knockdowns were performed in different cell lines. Trial experiments had revealed that increasing MOF expression beyond endogenous levels were detrimental for mitochondrial health. So, the rescue experiments were performed in a manner so as to have least increment of MOF levels.

To rescue a phenotype, the respective cell lines were induced by supplementing 0.1 µg/ml doxycycline (DOX, Sigma # D9891) in culture media for initial 48 hr of knockdown (D0 to D2, knockdown). This was followed by 48 hr of “recovery” in normal (DOX free) growth media. The specific assays on the cells were performed in the same manner as mentioned before in methods.

RNA-seq experiment on HeLa cells and mouse cardiomyocytes

RNA extraction and library preparation for HeLa cells

RNA was extracted using Trizol reagent (Life technologies #10296010) and treated with Turbo DNase (Life technologies #AM2238). Next, we enriched for mRNA (Poly A+) with Oligo dT magnetic beads, (RIN > 8). Finally, sequencing libraries were prepared using TruSeq stranded mRNA sample preparation kit (illumina #RS-122-2101).

RNA extraction and library preparation for mouse heart cardiomyocytes

Nuclear RNA of cardiomyocyte nuclei was prepared as previously described (Preissl et al., 2015). In brief, first cardiac nuclei were isolated from ventricular tissue. Next, cardiomyocyte nuclei were selected by staining with an anti-PCM1 antibody (Sigma #HPA023370) and sorted using a flow cytometer (Bio-Rad S3) (Gilsbach et al., 2014). Nuclear RNA was extracted using the RNeasy Micro Kit (QIAGEN # 74004). RNA was reverse transcribed and amplified with the Nugen Ovation RNA-seq System V2 (Nugen). The resulting cDNA was fragmented (Bioruptor, Diagenode). Sequencing libraries were constructed from 100ng fragmented cDNA using the NEBNext Ultra DNA Library Prep Kit (NEB) applying 9-13 PCR cycles. P15 cre-control (3 females and 2 males) and *Mof* KO (2 females and 1 male) mice were used in this study.

Analysis

Reads from RNA-seq analysis of human or mouse samples were mapped to the respective human (GRCh38) or mouse (GRCm38) genomes, using the STAR (v2.4.2a) aligner and counted for Ensembl transcripts (release 77 for Human and release 78 for Mouse) using feature Counts (v1.4.6-p2). Differential gene expression levels were determined using DESeq2 (v1.8.2). Genes were considered significantly different at a cut-off false discovery rate value of 0.05.

Gene set enrichment analysis was done using the GSEA software (v.2.2.1) using curated gene sets from Reactome, KEGG and HALLMARK.

Network maps were generated in Ingenuity Pathway Analysis (IPA, QIAGEN Redwood City, <https://www.qiagen.com/>), using curated lists from Ingenuity Pathways Knowledge Base. Global Molecular Network connections were used to generate relations between different pathways. The software used experiment-based knowledge to predict the effects of perturbation of individual molecules on the entire network. Causal network analysis (in IPA) was used to identify affected master regulatory pathways, based on the trends of known members of the network.

The accession number for the RNA-seq data reported in this paper is GEO: GSE77784.

Echocardiography

To assess cardiac function, mice were anaesthetized (2% v/v isoflurane in oxygen), placed on a temperature-controlled plate (37°C) and echocardiographic analysis was performed using a Vivid 7 Dimension ultrasound device (GE Medical Systems) equipped with an i13L transducer (14 MHz). Experiments were conducted on P16, control (9 females and 5 males) and KO mice (5 females and 3 males).

Histology and immunohistochemistry

Histology and immunohistochemistry was performed according to protocols mentioned before (Pfister et al., 2008). Briefly, hearts were fixed with 4% paraformaldehyde in phosphate buffered saline, embedded in paraffin, cut in 5 µm slices with a microtome (Leica) and stained. Histological staining with H&E or Sirius-red stain was performed. Cell membranes were labeled with Alexa Fluor conjugated wheat germ agglutinin (Molecular Probes #W11261, W21404). Nuclei were counterstained with DAPI (Molecular Probes #D1306) or Hoechst 33258 (Molecular Probes #H3569). Anti-H4K16ac (Millipore #07329) was used. Images were acquired with Zeiss Axio imager-Z1 with Apotome (Carl Zeiss) and were processed with Zen 2010 software (Carl Zeiss). Experiments were conducted on different sections of same P16, control (4 females and 4 males) and KO mice (5 females and 3 males).

Ploidy analysis of cardiomyocyte nuclei

Nuclei were isolated from cardiac tissue as previously described (Gilsbach et al., 2014). Cardiomyocyte nuclei were stained with anti-PCM1 antibody (Sigma) and DNA binding dye 7-AAD (7-aminoactinomycin D, Life technologies), before proceeding to flow cytometric analysis (Cy Flow Space, Partec, Germany).

Dihydroethidium (DHE) staining for ROS detection

Staining

Fresh tissue samples were snap frozen in chemically inert freezing medium (O.C.T. compound, VWR #361603E) and cryosectioned (20 µm) immediately before staining. Freshly made dihydroethidium (Thermo #D11347) solution was made freshly and used in 5 µM (in PBS) final concentration. Experiments were conducted on P10 (control- 2 females and 1 male; KO mice- 3 females) and P13 (control- 3 males; KO-1 female and 2 males) animals.

Image analysis

Confocal images of the tissue sections were acquired on LSM780 microscope (Carl Zeiss) using sequential channel acquisition. Images of tissue sections were analyzed with CellProfiler software with a customized pipeline from the website (<http://cellprofiler.org>). WGA staining channel served for identification of the cells; nuclei staining channel was used to identify nuclei; parameters of the identified nuclei were measured in DHE staining channel. At least 8 fields of view (340 × 340 µm) per sample were analyzed.

Electron microscopy

Mice were sacrificed by cervical dislocation and the heart and thigh musculature were harvested. Tissue blocks of 1 mm³ were prepared using a razor blade and fixed by immersion in 4% paraformaldehyde + 1% glutaraldehyde in 0.1 M phosphate buffer, for three days at 4°C. After the fixation, tissue blocks were washed in 0.1 M PB. After treatment with OsO₄, the sections were stained with uranyl acetate, dehydrated and flat-embedded in epoxy resin (Durcupan ACM, Fluka). 40 nm ultrathin cross- and longitudinal sections of the left ventricle and the skeletal muscle were cut and analyzed using an 80 kV Zeiss Leo transmission electron microscope. Experiments were conducted on P15, control (3 females and 2 males) and KO mice (3 females and 1 male).

Histone acetyl transferase (HAT) assay

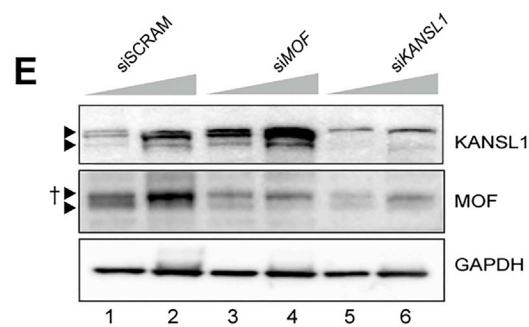
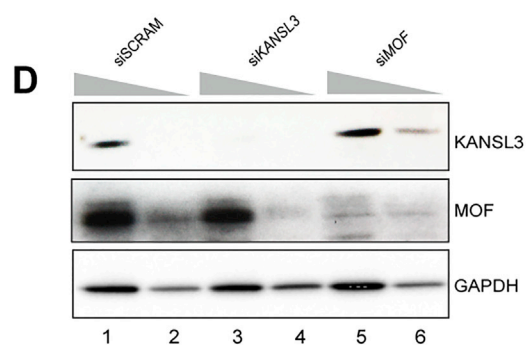
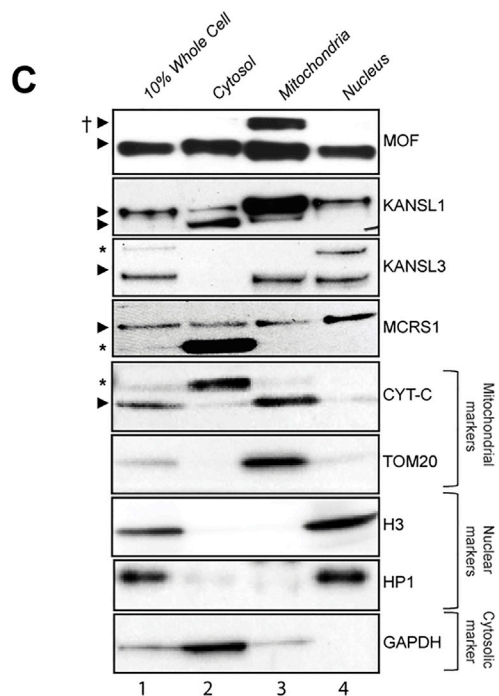
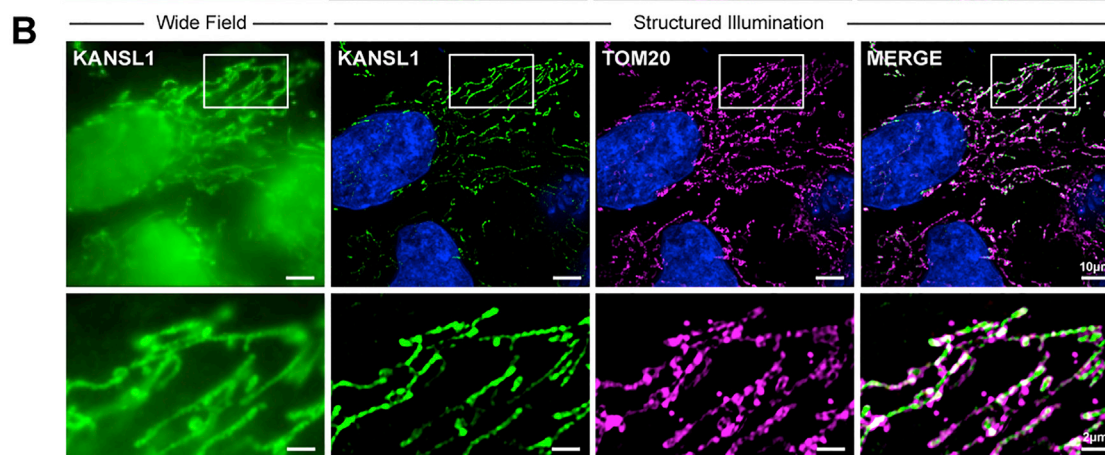
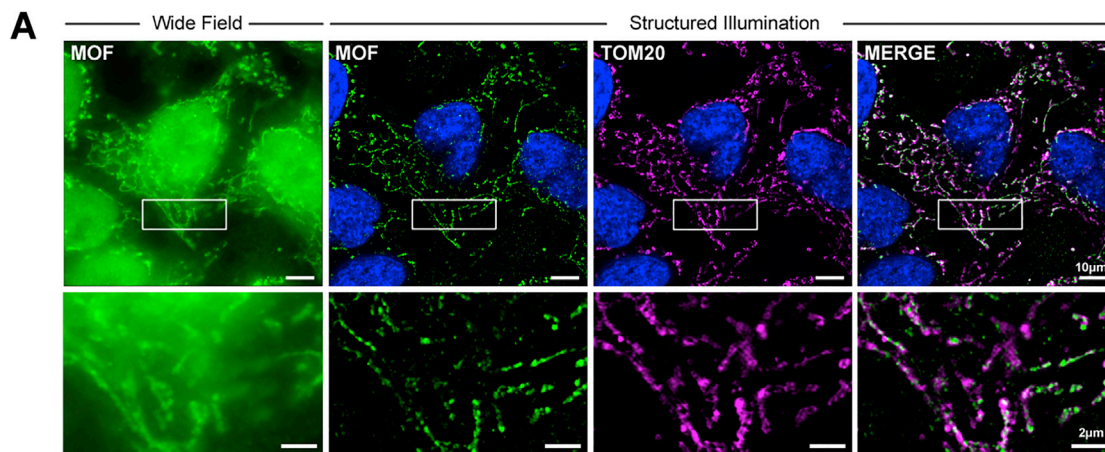
HAT assays were performed using baculovirus expressed human MOF-Flag, KANSL complex and MSL complex (described in [Meunier et al. \(2015\)](#)). Mono nucleosomes were reconstituted with bacterially expressed *Xenopus* histones and Widom 601 DNA (Active motif #53502) and HAT assays were performed as described before ([Akhtar and Becker, 2000](#)), with a minor modification. The assays were performed with 20 μM cold acetyl-CoA (Sigma #A2056) and data were analyzed by western blots.

QUANTIFICATION AND STATISTICAL ANALYSIS

Data are presented as mean ± SE or SD. Each experiment was performed with a minimum of three biological replicates; exact numbers are mentioned in associated figure legends. Except RNA-seq analysis, all statistical analyses were performed using Prism 6 software (GraphPad). The statistical tests used and relevant p values are mentioned in appropriate figures/figure legends. p values < 0.05 were considered significant.

DATA AND SOFTWARE AVAILABILITY

The accession number for the RNA-seq data reported in this paper is GEO: GSE77784.



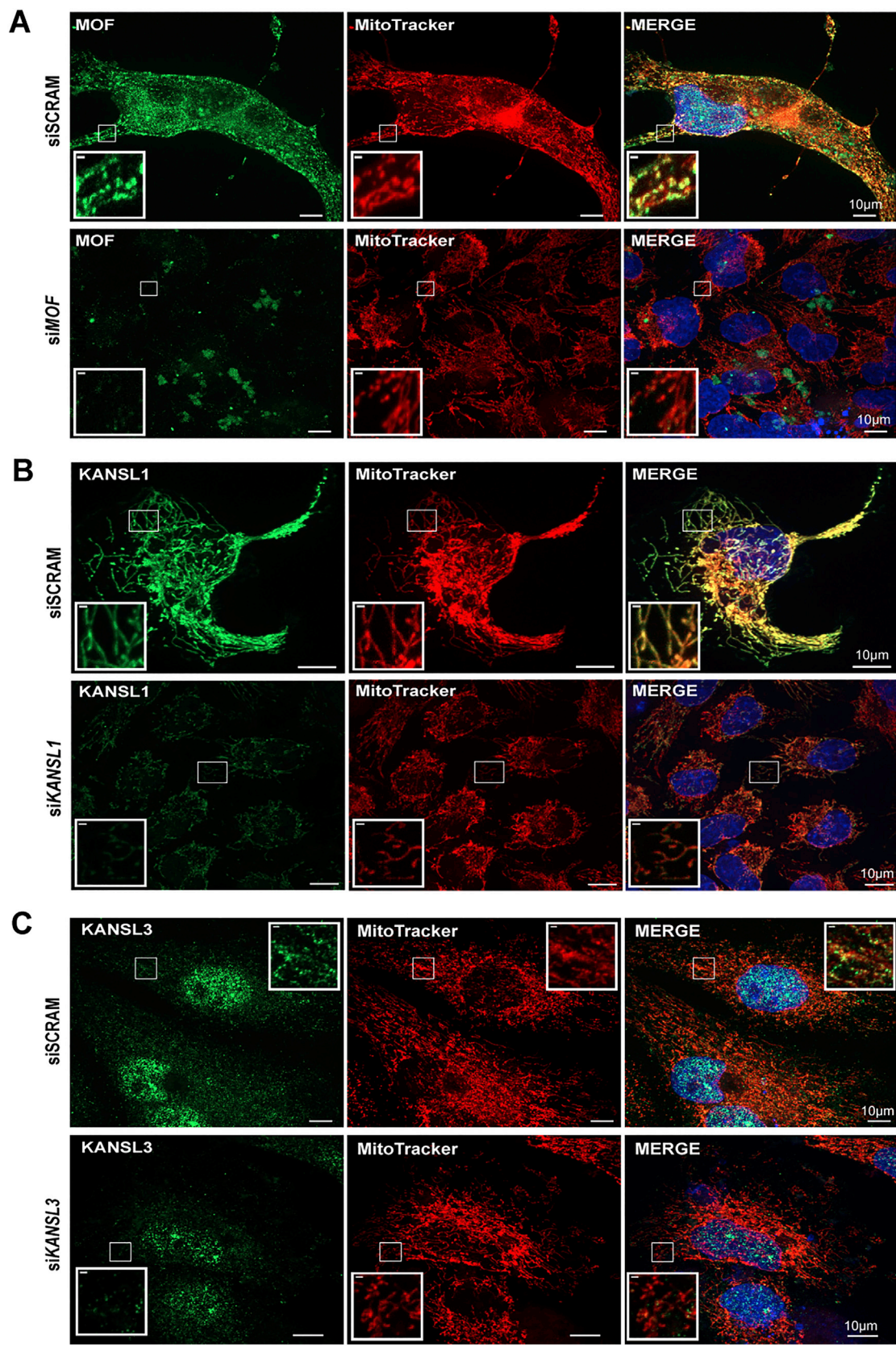
(legend on next page)

Figure S1. MOF and KANSLs Localize to Mitochondria, Related to Figure 1

(A and B) 3D structured illumination microscopy (SIM) of HeLa cells immunostained with (A) anti-MOF (B) anti-KANSL1 (green) along with anti-TOM20 (magenta) for mitochondria and DAPI (blue) for nucleus. Merged image sets represent combination of all three channels. Wide field fluorescence image of the (MOF/KANSL1 staining, green) is shown in first column of (A) and (B). Scale bars are mentioned within. The enclosed area within each image is shown at a higher magnification below it.

(C) Biochemical fractionation of HeLa cells followed by probing with MOF, KANSL1, KANSL3 and MCRS1 specific antibodies. Quality of each fractionation was confirmed by observation of well-known marker proteins for each fraction; cytosol (GAPDH), mitochondria (TOM20, CYT-C) and nucleus (H3, HP1). Triangles denote specific protein band and a cross is added to indicate isoform or post-translationally modified version of the protein. Asterisks mark unknown bands enriched predominantly in mitochondrial purifications.

(D and E) Knockdown experiments followed by western blots to show specificity of MOF, KANSL1 and KANSL3 antibodies. The specificity of the annotated bands for each antibody was determined by observing loss of signal upon depletion of the respective protein. All experiments were performed in parallel after 3.5 days of siRNA treatment. Triangles denote specific bands (knockdown sensitive). For, MOF additional cross denotes an isoform or post-translationally modified version, mentioned before in [Figures 1D](#) and [S1C](#).



(legend on next page)

Figure S2. Validation of MOF, KANSL1, and KANSL3 Immunofluorescence Signals, Related to Figure 1

(A–C) Confocal images of cells treated with control (siSCRAM) and siRNA (siMOF/KANSL1/KANSL3) to assess sensitivity of immunofluorescence signals to the respective protein depletion. Scale bars of main figures are mentioned within. The enclosed area within each image is shown at a higher magnification as an inset in the same. For insets, scale bars represent 1 μm .

(A) HeLa cells stained with MOF (green), MitoTracker (red) and DAPI (blue). Top panel- siSCRAM cells. Bottom panel- siMOF cells.

(B) HeLa cells immunostained with KANSL1 (green), Mitotracker (red) and DAPI (blue). Top panel- siSCRAM cells. Bottom panel- siKANSL1 cells. The cells have been imaged with $\sim 50\%$ KANSL1 depletion as higher knockdown efficiency triggers mitochondrial degeneration, making it difficult to determine signal specificity.

(C) HeLa cells stained with KANSL3 (green), Mitotracker (red) and DAPI (blue). Top panel- siSCRAM cells. Bottom panel- siKANSL3 cells. The cells have been imaged with $\sim 50\%$ – 60% KANSL3 depletion, as higher knockdown efficiency triggers mitochondrial degeneration.

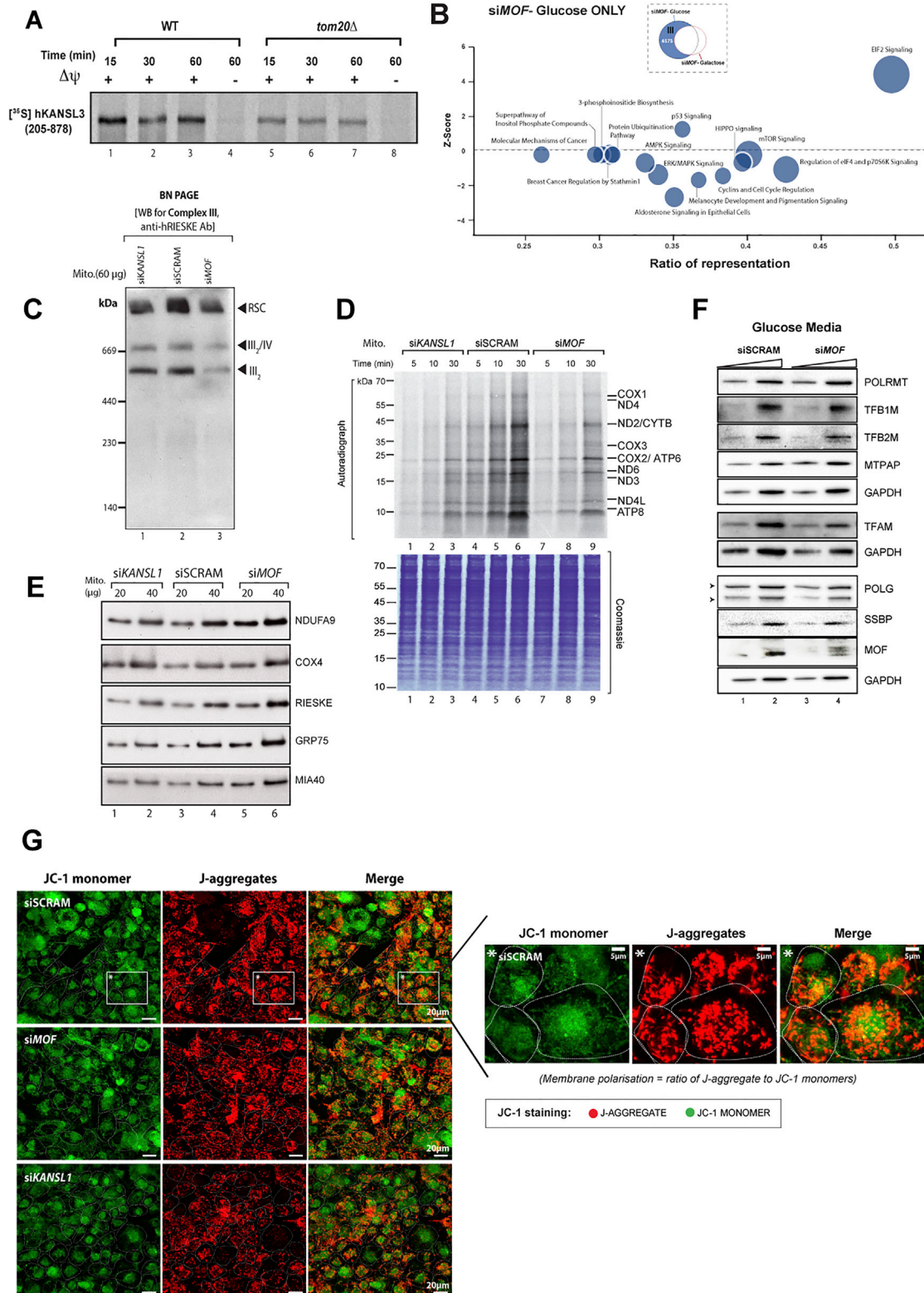


Figure S3. Physiological Impact of MOF and KANSL1 Depletion, Related to Figures 1 and 2

(A) [³⁵S] KANSL3 (205-878) was imported into WT or *tom20Δ* yeast mitochondria for the indicated periods. The assay was performed with polarized (+ $\Delta\psi$) as well as depolarized ($-\Delta\psi$) mitochondria. Non-imported proteins were removed by proteinase K.

(legend continued on next page)

(B) Bubble plot showing top fifteen significantly affected pathways, exclusively in galactose media (III, from [Figure 2A](#)) after MOF depletion. The y axis shows Z score of enrichment and the x axis indicates the ratio of representation of genes from a particular pathway in our dataset. Finally, size of the bubble is directly proportional to level of significance of discovery ($-\log_{10}$ p value).

(C) Immunoblotting of mitochondrial extracts from siSCRAM, siMOF and siKANSL1 samples separated by blue native (BN) PAGE. The BN-PAGE was probed with antibodies against respiratory complex I (NDUFA9), complex III (Rieske) and complex IV (COX4) proteins. RCS, respiratory chain supercomplexes; MIA, mitochondrial intermembrane space import and assembly machinery.

(D) In organello translation of purified mitochondria from siSCRAM, siMOF and siKANSL1 cells. Top, autoradiograph of mitochondria-synthesized polypeptides is shown. Bottom, Coomassie stained image of the same gel is shown below for loading estimation. KDa represents molecular weight markers. Assay time is indicated in minutes (min).

(E) Immunoblotting of mitochondrial extracts from siSCRAM, siMOF and siKANSL1 samples by SDS-PAGE. Plots were probed with antibodies against NDUFA9, Rieske and COX4. GRP75 and MIA40 were used as loading controls.

(F) Immunoblotting of cell extracts from siSCRAM and siMOF glucose adapted samples. Blots were probed with antibodies against mtDNA transcription (TFAM, POLRMT, TFB1M, TFB2M and MTPAP), mtDNA replication (POLG and SSBP) in addition to MOF and GAPDH (loading control).

(G) JC-1 staining of siSCRAM, siMOF and siKANSL1 cells. Enlarged view of the enclosed region is shown on right.

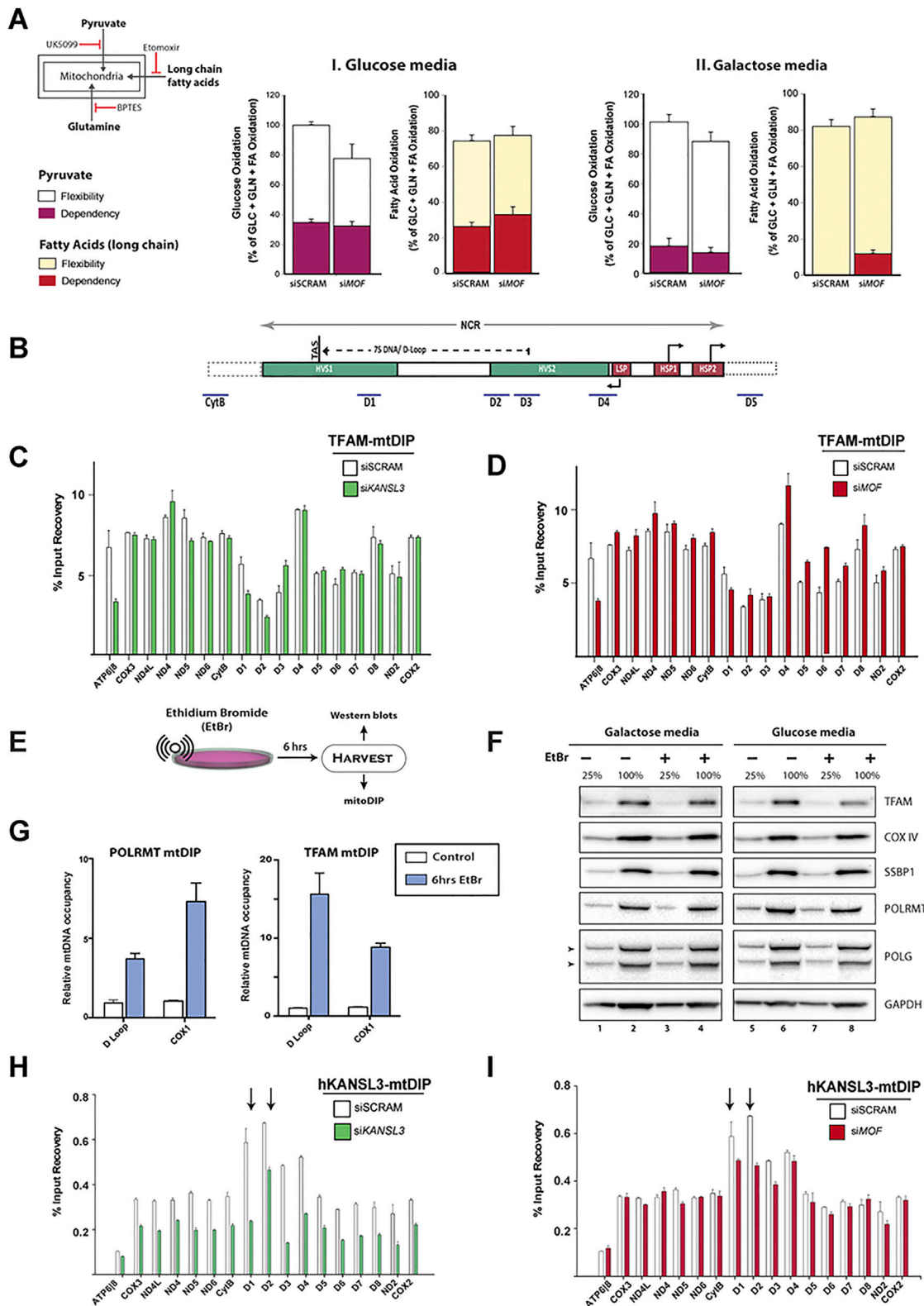


Figure S4. MOF and KANSL3 Associate with mtDNA, Related to Figures 2 and 3

(A) Respirometry assays performed to identify cellular dependency on nutrient sources. Experiment involved injection of inhibitors blocking import of major nutrients to mitochondria, in control (SCRAM) and *siMOF* samples. Parallel knockdowns were performed on HeLa cells either adapted to glucose or galactose (legend continued on next page)

media. On left, a schematic is presented showing the action of different drugs used in the assay. UK5099 blocks pyruvate transport to mitochondria; BPTES blocks glutaminase 1 (transporter of glutamine into mitochondria); Etomoxir blocks CPT1 mediated long chain fatty acid transport into mitochondria. Dependency reflects the reliance of cells on a particular nutrient to maintain basal respiration. Flexibility denotes the ability of a cell to increase oxidation of a particular fuel type, to meet metabolic demands of the cell or compensate for inhibition of an alternate fuel source. Specific nutrient oxidation capacity is represented as a percentage of total respiration from all three major nutrient sources- glutamine (gln), glucose (glc) and fatty acids (FA). Data represent mean \pm SD of 3–5 biological replicates. (B) The cartoon from [Figure 3G](#) is re-represented in this figure for mtDIP reference in next section. It shows a detailed representation of the non-coding region (NCR) of human mtDNA with corresponding primers from the region is shown below the graph. TAS = Transcription associated site; HVS1/2 = Hyper variable site 1/2; LSP = Light strand promoter; HSP1/2 = Heavy strand promoter 1/2. (C and D) TFAM mtDIP-qPCR performed in control (siSCRAM, white) and (C) siKANSL3 (green) or (D) siMOF (red). The selected targets effectively cover the entire human mitochondria and mtDIP efficiency is calculated as percentage of input recovery. Data are representative of three biological replicates. Error bars denote \pm SEM. (E–G) Impact of brief exposure to ethidium bromide (EtBr) on mitochondrial transcription. (E) Schematic overview of the experimental scheme is presented. (F) Western blotting for different mitochondrial transcription (TFAM and POLRMT) and replication (SSBP1 And POLG) factors. GAPDH and COX IV were used as loading controls. (G) mtDIP assay for POLRMT and TFAM, followed by qPCR for two loci on mtDNA- the D-loop and the COX1 region. Data are represented as relative mtDNA occupancy over control samples, using three biological replicates. Error bars denote \pm SEM. (H and I) Similar to [Figures S4B–S4D](#), KANSL3 mtDIP-qPCR performed in control (siSCRAM, white) and (H) siKANSL3 (green) or (I) siMOF (red). The selected targets effectively cover the entire human mitochondria and mtDIP efficiency is calculated as percentage of input recovery. Data are representative of three biological replicates. Error bars denote \pm SD.

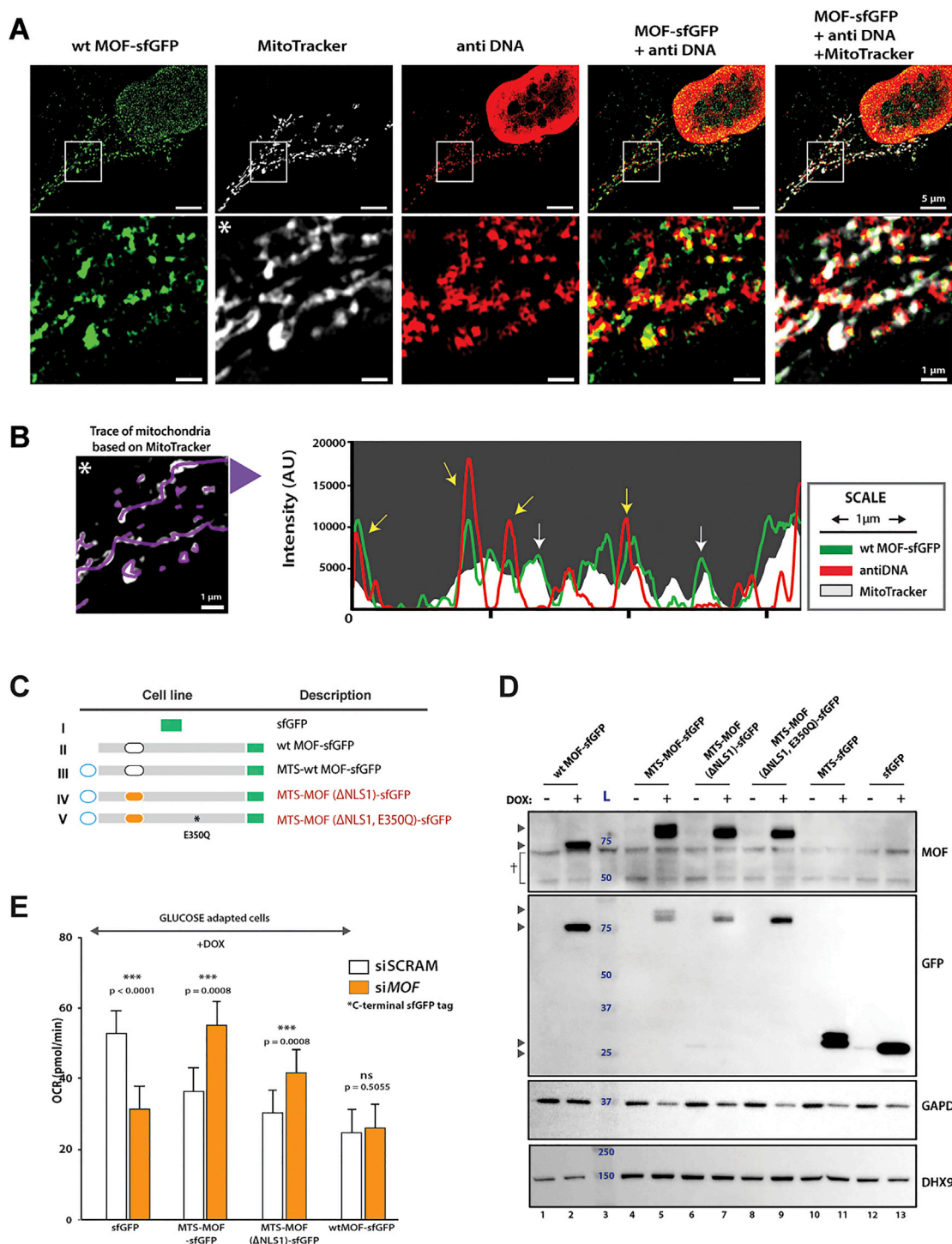


Figure S5. Functional Assays Characterizing Effect of MOF in Mitochondria, Related to Figures 3 and 4

(A) 3D high resolution (HR) structured illumination microscopy (SIM) of HeLa cells expressing wtMOF-sfGFP (green), co-stained with MitoTracker (white) and anti-DNA (red). Magnified view of enclosed region is shown below.

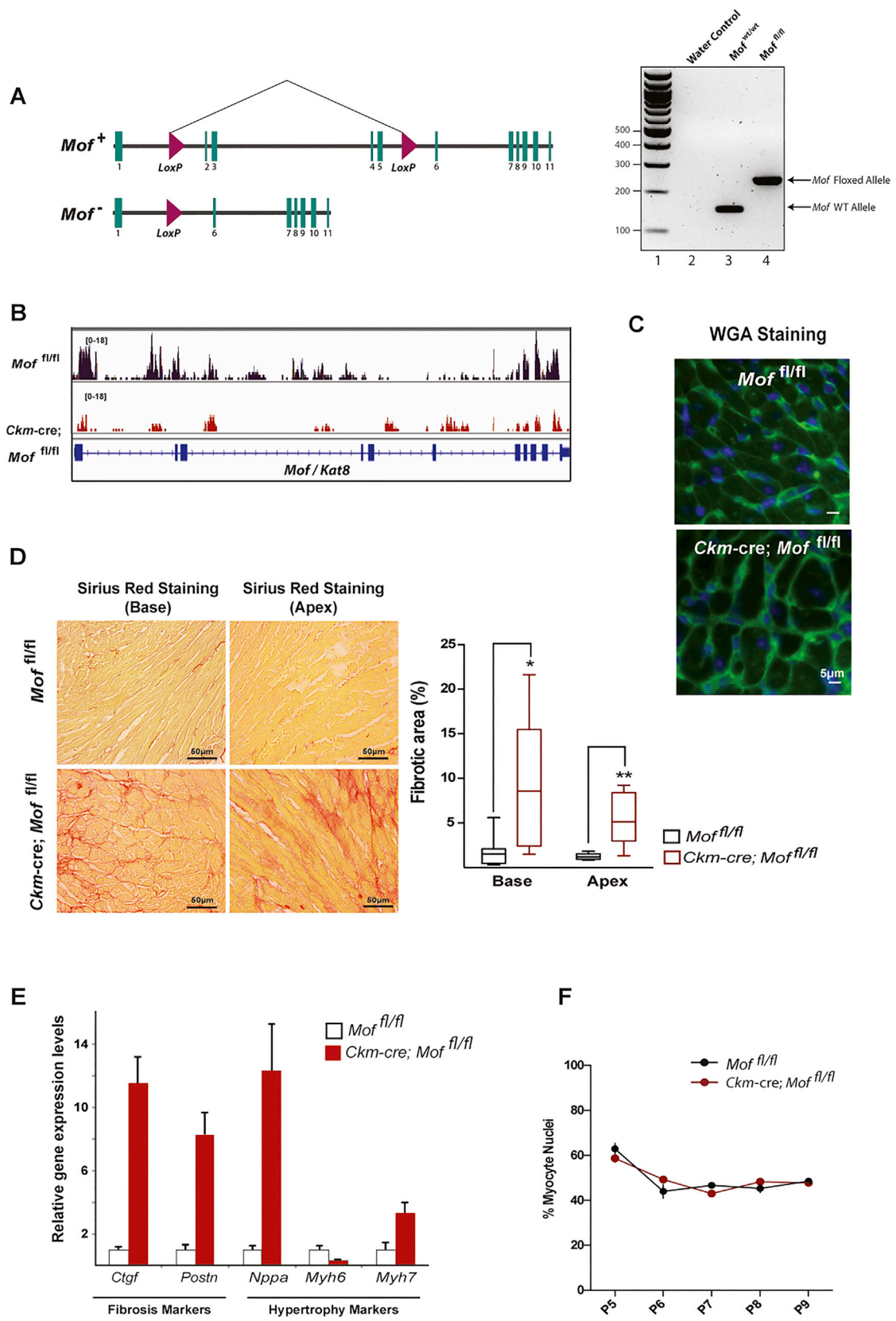
(B) The mitochondria (white) from Figure S5A is traced (purple line overlaid on white) and histogram of three channels, wtMOF-sfGFP (green), mitochondria (white) and DNA (red) is shown next to it. Yellow arrows = overlap of all three channel signals. White arrows = overlap of MOF and MitoTracker signal.

(C) Schematic illustrations of the doxycycline (DOX) inducible cell lines used in rescue experiments. Features represented: COXIV mitochondrial-targeting signal (MTS, blue ellipse); MOF (gray thick line); MOF's nuclear localization signal 1 (NLS1, black ellipse) and its mutated form (Δ NLS1, orange filled ellipse); sfGFP (green filled rectangle); asterisks indicate point mutation (E350Q) in MOF's HAT domain.

(legend continued on next page)

(D) Western blots showing doxycycline dependent induction of different sfGFP tagged cell lines used in the manuscript. Blots are probed for MOF and GFP antibodies. GAPDH and DX9 are used as loading controls. "+" = Overnight induction with 0.1 $\mu\text{g}/\text{mL}$ Doxycycline, "-" = uninduced cells. MTS = COX4A mitochondrial targeting signal. Triangles, sfGFP tagged transgene. Cross, the endogenous protein bands. L= molecular weight ladder in kDa.

(E) Respiratory rescue experiments of glucose adapted cell lines. Basal respiration is calculated from the respirometry profile of the cell lines after control (siSCRAM) or siMOF treatment. Five biological replicates were used and samples were induced with doxycycline (DOX). Two tailed t test with Welch's correction, p values are mentioned in the figure. Error bars represent \pm SEM.



(legend on next page)

Figure S6. *Mof* KO Mice Display Classical Signs of Cardiac Hypertrophy, Related to Figure 6

(A) Strategy used to generate *Mof*-floxed locus. On right, an agarose gel for genotyping, showing the WT and floxed (fl) *Mof* locus using specific PCR primers. (B) Consistent with Figure 7A, RNA-seq analysis shows reduction in nuclear *Mof* RNA, in *Mof*^{fl/fl} (control, black) versus *Mof*^{fl/fl}; *Ckmm*-cre (KO, red) mice. x axis represents mouse *Mof* gene.

(C–F) Cardiac phenotyping of *Mof*^{fl/fl} (control) and *Mof*^{fl/fl}; *Ckmm*-cre (KO) mice. (C) Wheat germ agglutinin (WGA) stained sections of control and KO mouse hearts. WGA stains cell membranes (green), while nuclei are stained with DAPI (blue). The larger hollow cells in each section are cardiomyocytes.

(D) Histochemical staining of left ventricular cardiac sections from control and a KO mouse with Sirius red, which stains collagen, and was used to quantitate interstitial fibrosis by morphometry. Right, representation of interstitial fibrosis calculated from base and apex of hearts based on Sirius red staining, in control (black box, n = 8) and KO (red box, n = 8) animals. Error bars represent ± SEM. Unpaired t test, **p = 0.0035, *p = 0.0126.

(E) Relative mRNA expression of marker genes for fibrosis (*Ctgf* and *Postn*) and hypertrophy (*Nppa*, *Myh6* and *Myh7*) from control (white bar, n = 14) and KO (red bar, n = 8) mice. *Rps29s* expression was used as internal standard. Error bars represent ± SEM.

(F) Percentage of cardiomyocyte nuclei in heart ventricle tissue of control (black line) and KO (red line) animals, followed from P5-P9 after birth, (n = 3-4) in each time point. Control also included *Ckm*-cre; *Mof*^{fl/+} and *Mof*^{fl/+}. Error bars represent ± SEM.

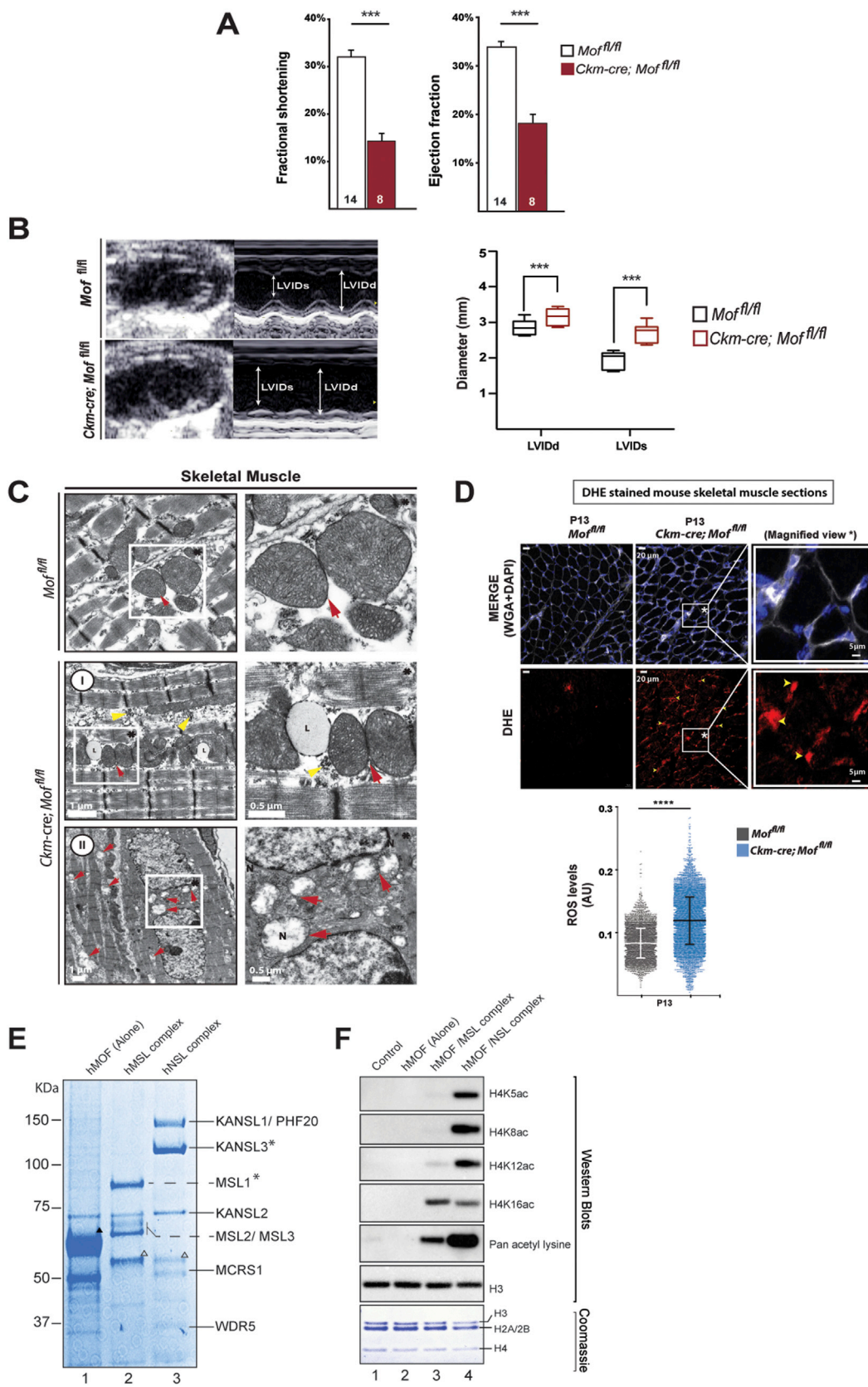


Figure S7. Characterization of *Mof* KO Mice Display Classical Signs of Cardiac Hypertrophy, Related to Figures 6 and 7

(A) Cardiac contractile function determined by echocardiography as left ventricular fractional shortening (left) or ejection capacity (right), in control (white bar, n = 14) and KO (red bar, n = 8) mice. Error bars represent \pm SEM. Mann-Whitney U test, ***p < 0.005.

(B) Echocardiogram showing left ventricular inner diameter (LVID) changes during systole- LVIDs and diastole- LVIDd. The box plots on right show the numerical values of changes in the diameter, in control (black box, n = 14) and KO (red box, n = 8) animals. Error bars represent \pm SEM. Mann-Whitney U test, ***p < 0.005.

(C) Electron micrographs of skeletal muscle tissue sections from P15 mice- *Mof*^{fl/fl} (control, n = 5) and *Mof*^{fl/fl}; *Ckm-cre* (KO, n = 4) mice. The top panel is representative of skeletal muscle from control animals (*Mof*^{fl/fl}). (I-II) Range of phenotypes observable in KO skeletal tissue samples (*Ckm-cre*; *Mof*^{fl/fl}): (I) Skeletal muscle section showing normal tissue morphology, with only mild elevation in lipid deposition (L). A magnified view of enclosed region is shown on right, slight deposition of glycogen (yellow triangle) and normal mitochondria (red arrow) is observed. (II) Specialized muscle spindle in the skeletal tissue, with intact nuclei (N) but degenerated mitochondria (red arrows), elevated deposition of lipids (L). Magnified view of enclosed area is presented on right.

(D) Dihydroethidium (DHE) stained skeletal muscle sections of P13 control (*Mof*^{fl/fl}) and MOF-KO (*Ckm-cre*; *Mof*^{fl/fl}) mice (n = 3, for each genotype). The mean fluorescence signals were calculated from multiple images of each sample set and represented as relative ROS level in a.u. Yellow triangles indicate DHE/ROS accumulation. Error bars represent \pm SEM. Unpaired t test, ***p < 0.005.

(E) Coomassie stained gel of purified hMOF, hMSL complex (MOF, MSL1, MSL2 and MSL3) and hNSL complex (MOF, KANSL1, PHF20, KANSL2, KANSL3, MCRS1 and WDR5), expressed in baculovirus-infected insect (sf21) cells. Dark triangle represents flag tagged MOF. Open triangles denote untagged MOF. Asterisks indicate the Flag-tagged protein used for pull-down/purification. kDa represent the molecular weight ladder.

(F) HAT assays performed on reconstituted nucleosomes with purified hMOF, hMOF/MSL and hMOF/NSL complex. Control assay was performed in identical conditions, but without enzyme (hMOF). Coomassie stained gel at the bottom displays histone content of the nucleosomes used.